1. High-performance AlGaN Ultraviolet Photodetectors

High-performance AlGaN Ultraviolet Photodetectors

----Development for application of flame sensing

Abstract

This research work, aiming to develop high performance AlGaN ultraviolet (UV) photodetectors for the application of flame sensing, is a part of the project "Intellectual Cluster Headquarters: Development of high-performance nano-sensor and materials" supported by Intellectual Cluster Headquarters, Aichi Science & Technology Foundation. The progress of the research activities can be divided into three phases: (1) performance improvement of GaN UVA photodiodes on sapphire substrates, (2) development of high-performance flame sensing $Al_{0.23}Ga_{0.77}N$ UVB photodiodes on AlN/sapphire templates, and (3) development of high-performance flame sensing solar-blind $Al_{0.4}Ga_{0.6}N$ UVC photodiodes on 4H-SiC substrates and AlN/sapphire templates. In the first phase of the project, the most improved performance was observed in the GaN UVA Schottky photodiodes with Ir/Ni/Ir Schottky electrodes which demonstrated low dark current density (J_d) of 1.8×10^{-10} A/cm^2 at -5 V, zero-bias external quantum efficiency (*EQE*) of 38%, and estimated specific detectivity (D^*) of 5.8×10^{15}cmH$^{1/2}$/W at 350 nm and 296 K. In the second phase, the AlN/sapphire templates were employed as substrates. A high-temperature GaN interlayer was introduced to reduce the threading dislocations in the AlGaN active layer. With the reduced dislocation density, the fabricated $Al_{0.23}Ga_{0.77}N$ UVB Schottky photodiodes exhibited excellent performance with parameters of J_d =3.3×10^{-11} A/cm^2 at -5 V bias and zero-bias *EQE*~26% at 310 nm. By using the large-active-area (4×4 mm^2) photodiodes, we have detected the UV signal from the lighter flame and then confirmed their capability for being used as flame sensor. In the third phase, we have achieved high-performance solar-blind $Al_{0.4}Ga_{0.6}N$ UV photodetectors in both of the Schottky and *p-i-n* structures. The fabricated photodiodes demonstrate J_d ~10^{-11} A/cm^2 at -5 V bias, zero-bias *EQE*~20% at 258 nm, and D^*~7.0×10^{14}cmH$^{1/2}$/W. The capability for detecting lighter flame was also verified on these solar-blind photodiodes.

1. Introduction

The advances in the crystal growth and optoelectronic device fabrication of III-nitride wide-band gap semiconductors has led to the commercialization of bright blue, green, and white light-emitting diodes as well as blue laser diodes for display and data storage applications. There is also significant research underway in the area of III-nitride based high temperature, high power electronics and microwave devices. Recently, research interest has grown in using this material system to fabricate UV photodetectors (PDs). The potential applications of UV PDs include biological and chemical sensing, flame detection, UV emitter calibration, secure space-to-space communications, and early plume detection of missiles or aircraft engines, etc.

The $Al_xGa_{1-x}N$ material system has a number of advantages, making it one of the most suitable materials for fabricating UV PDs. By changing the Al composition, x, from 0 to 1, its band-gap energy (cutoff wavelength) can be tailored from 200 to 365 nm. The large band-gap is beneficial for obtaining low dark current because of low thermally generated noise. Moreover, its chemical, mechanical and thermal stability makes this material suitable for operation in harsh environments.

The object of this research project is to develop the high-performance AlGaN UV PDs used as flame sensor. Currently, UV photomultiplier tube (PMT) is the mainstream technology with the highest performance for flame detection. These detectors can provide extremely low dark current, high responsivity, and large internal gain. However, PMTs are fragile, bulky, and require high operation voltages. In addition, for the applications of UV detection, PMTs have to be integrated with expensive and complex filters due to their high response in the visible range. Therefore, it is highly desired to alternative PMTs with solid-state UV PDs, which are low cost, compact, robust, and low-voltage operation.

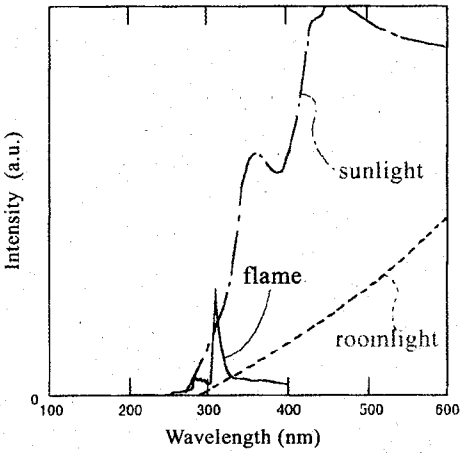

FIG. 1.1. Spectra of the sunlight, room light, and gas falme.

For being used as flame sensor, the following

elements are required for the AlGaN UV PDs. (1) high rejection to the background radiation noise (solar or room light) is necessary (see Fig. 1.1); (2) to detect the weak UV signal from the flame with intensity level of ~nW/cm^2, the AlGaN PD should have the low dark current with a density of ~10^{-11}A/cm^2 at the operating voltage and temperature; and (3) high responsivity (>10 A/W) is needed so that the generated photocurrent is large enough for the photodiode amplifier circuit .

It is known that the ultraviolet spectrum can be divided into three basic sub-regions: **UVA** (320-400 nm), **UVB** (280-320 nm), and **UVC** (100-280 nm). In these spectrum regions, UVC range is of special interest. The UVC radiation is strongly absorbed by the terrestrial ozone layer and atmospheric oxygen, so that almost no UVC radiation reaches the earth's surface. Accordingly, the photodetecters operating in this spectral range will not see a large background signal from the solar radiation and be capable to detect very weak UV signal. For achieving high visible/solar rejection, developing AlGaN photodetectors operating in UVC (solar-blind) region is then one of the targets of our research work.

Besides the solar-blind characteristics, we need to get low dark current and high responsivity in AlGaN PDs. Achieving these performances depends on a series of factors including the epitaxial crystalline quality, *p*-type and *n*-type doping efficiency, electrode contact technology and device fabrication and design. At present stage, a major obstacle for high performance AlGaN PDs is the high defect density of AlGaN layers. Threading dislocations and point defects play a very important role in the performance characteristics of AlGaN PDs. It has been shown that threading dislocations, in particular, screw dislocations, are a primary source of leakage in AlGaN Schottky and *pn* junctions. Therefore, as shown in this report, reducing dislocation density and suppressing leakage (dark) current in AlGaN PDs are an essential component of our research.

The requirement of high UVC responsivity (>10 A/W) means that the internal gain due to avalanche multiplication is needed for our AlGaN PDs used as flame sensors. Since the state of art for the defect density of $Al_xGa_{1-x}N$ (x>0.4 for solar blind) is still much high (~10^9-10^{10} /cm^2, for line defect density), to realize solar-blind AlGaN avalanche photodiodes presents the most challenging task in this project for us.

2. GaN UVA MSM Schottky & Schottky photodiodes

--performance improvements with novel device structure

2.1 Epitaxial growth and experimental procedure

The epitaxial layers used for UVA photodiodes were grown by *atmospheric-pressure* (AP) metal organic chemical vapor deposition (MOCVD) using a *NIPPON SANSO SR2000* system on (0001)-plane sapphire substrates. The precursors used were NH_3 and the trimethyl compounds of aluminum (TMA) and gallium (TMG), while the carrier gas was purified hydrogen. Monosilane (SiH_4) was used as dopant source for *n*-type (Si) incorporation and Cp_2Mg was used as dopant source for *p*-type (Mg) doping. The substrates were first heated to 1230 °C for 10 min in H_2 ambient for in-situ cleaning. The temperature was then lowered to 500 °C to deposit a 30-nm-thick GaN nucleation layer under $NH_3/N_2/H_2$ ambient condition. The subsequent epilayers for comprising detector structure were all grown at 1180 °C.

For device performance analysis, an Agilent 4156C precision semiconductor parameter analyzer was used for the current–voltage (*I-V*) measurements. The capacitance-voltage (*C-V*) measurements were carried out at test frequency ranging from 20kHz to 1MHz using an HP4284 LCR meter. Spectral responsivity measurements were performed in the range of 500~300 nm using a UV-visible spectrophotometer (JUSCO CT25 GT/GD), which consists of a light source comprising a quartz halogen lamp and a xenon-arc lamp, a monochromator, and a current source-measure unit. The optical system is calibrated by a UV-enhanced Si detector. The irradiation power density was corrected by a thermopile detector and kept at 10 $\mu W/cm^2$ in the entire measuring range. All measurements were performed at room temperature.

2.2 UVA MSM PDs based on undoped AlGaN/GaN HEMT structure

The AlGaN/GaN heterostructure has recently been the subject of intense research for application in high-temperature/high-power electronic devices and optoelectronic devices.[1,2] The first UV photodetector based on the AlGaN/GaN heterostructure was

reported by Khan *et al.*,[3] in which the heterostructure field-effect transistor (HFET) was used as the gated visible-blind photoconductor. This type of photodetector showed the advantages of high gain and monolithical integration with field effect transistor (FET) circuits in one epitaxial step. A major drawback of this photoconductivity detector is, however, the relatively large dark current, which limits the minimum detectable irradiation power. Schottky MSM-PDs are attractive devices because of their low dark current, high response speed, superior responsivity, and simple planar structure which is compatible with the FET fabrication process. It is well known that piezoelectric and spontaneous polarization fields occurring in AlGaN/GaN heterostructures grown by MOCVD can generate a high two-dimensional electron gas (2DEG) density at the heterojunction interface without the doping procedure.[4] For this reason, the undoped AlGaN/GaN structure can also be used for HEMT fabrication.[5] It is then promising to fabricate the Schottky MSM-PDs on the undoped AlGaN/GaN heterostructures, enabling the monolithical integration of MSM-PDs in HEMT circuits in one epitaxial step, while maintaining the MSM-PDs' own superior performance. In this work, we investigated the MSM-PDs prepared on the undoped AlGaN/GaN heterostructure under illumination from either the top or the back.

The epilayer structure was consisted of a 30 nm GaN nucleation layer on a (0001) sapphire substrate followed by a 0.8 μm undoped *i*-GaN buffer/channel layer, a 20 nm undoped *i*-$Al_{0.17}Ga_{0.83}N$ barrier layer and a 7 nm *i*-GaN cap layer.

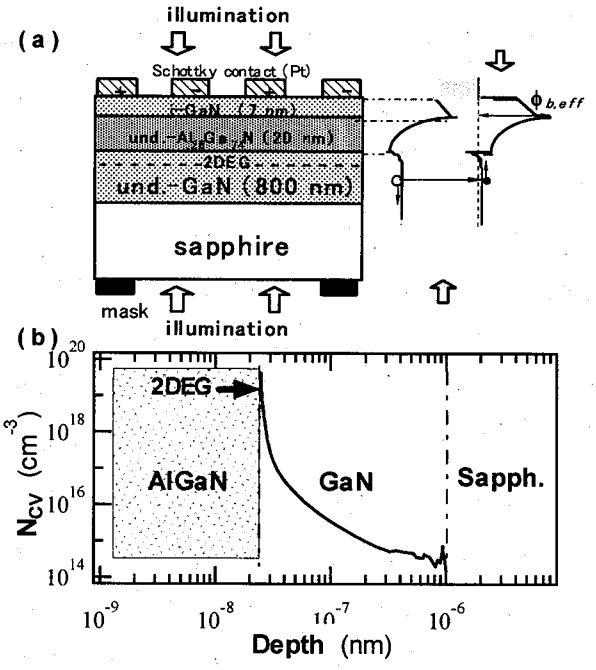

FIG. 2.1. (a) Schematic diagram of the device and its energy band. A 7-nm-thick i-GaN cap layer is used to enhance Schottky barrier height (SBH) and hence to suppress the leakage current according to the data of **ref.** 6. (b) C-V concentration profile of the AlGaN/GaN heterostructure measured from a planar Schottky diode with Pt Schottky dot and Ti/Al/Ni/Au ohmic guard ring.

By Hall-effect measurement, the electron mobility was found to be 909 cm^2/Vs at 300 K and 4208 cm^2/Vs at 77 K, respectively, and the sheet carrier density was found to be $3.2\times10^{12}cm^{-2}$ at 300 K. Figure 2.1(a) shows

the schematic structure of the device with the energy band diagram. Interdigital patterns with the active area of 100×105 μm^2, finger width of 5 μm, and gap spacing of 5 μm were defined by photolithography. Semitransparent Schottky contacts were formed with a 100-Å-thick Pt layer, and a Ni/Au (20/300 nm) bilayer was deposited as contact pads. The carrier concentration profile of the GaN/AlGaN/GaN heterostructure, as shown in Fig. 2.1(b), was determined by *C-V* measurement at 20 kHz. The profile demonstrates that the 2DEG is confined to the lower AlGaN/GaN interface.

Figure 2.2 exhibits the *I-V* characteristics of the fabricated heterostructural MSM-PD. The dark current of this device will be determined by the cathode depletion region which shares the largest portion of the applied voltage and limits the dark current to the greatest degree. As depicted in Fig. 2.2, the dark current shows a strong voltage dependence at low bias voltages ($0<V_b<1.9$ V) and a plateau at high bias voltages ($V_b>1.9$ V), where 1.9 V is the bias voltage when the 2DEG channel below the cathode depletion region is pinched off, as will be shown later. This current behavior is exactly the same as that of gate leakage of the AlGaN/GaN heterostructure HEMT reported by Miller *et al.*[7] On the basis of ref. 7, it can be speculated that the dark current in the present experiment is due primarily to vertical tunneling through the potential barriers at the AlGaN/GaN heterointerface and at the Schottky contact between the AlGaN barrier layer and the cathode metal. At a typical bias of 10 V, the current amounts only to 2.4 pA, which corresponds to a current density of 1.8×10^{-8} A/cm^2 using the metal contact area as the effective area. We attribute the low dark current to the *i*-GaN cap layer, which piezoelectrically enhanced the effective SBH.[6] The introduction of such a cap layer showed that it reduced the leakage current density by more than two orders of magnitude, as compared with that of the samples without the cap layer (not given in Fig. 2.2).

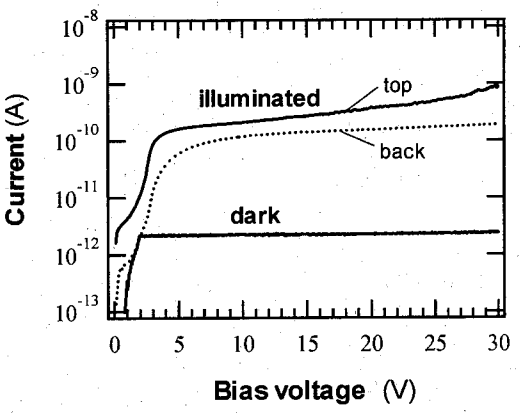

FIG. 2.2. Dark and illuminated I-V characteristics of the AlGaN/GaN heterostructure MSM-PD.

The photocurrents were measured under the illumination of 25 $\mu W/cm^2$ with a wavelength of λ=350 nm from the top and back. When the incident photon energy is equal to or larger than the GaN band gap (E_g^{GaN}) but less than the AlGaN band gap (E_g^{AlGaN}), the AlGaN layer is almost transparent to the incident photons from the top, and the dominant photoeffect is the generation of electron-hole (*e-h*) pairs in the GaN channel layer. The photogenerated carriers tunneling through the potential barriers at the heterointerface and Schottky contact contribute to the photocurrent. It should be pointed out that the photoelectrons generated near the 2DEG channel will experience a built-in electric field associated with the band bending at the heterostructure interface, as shown in Fig. 2.1 (a). By this electric field, the photoelectrons are forced into the 2DEG channel, contributing to an increase in the charge density of 2DEG. The result is an increase in the electric field at the heterointerface, which leads to enhanced band bending. This effect, however, is expected to occur generally at the anode contact side. As the applied bias increases, the 2DEG channel below the cathode contact tends to be pinched off and the energy band of the GaN channel layer at the heterointerface tends to become flat. Once the 2DEG beneath the cathode contact is depleted, the channel resistance increases and absorbs the additional applied bias. The photocurrent saturates and becomes less dependent on bias voltage. For illumination from the back, the device exhibits a smaller photocurrent due to the recombination loss of the photoexcited *e-h* pairs in the GaN channel layer. For illumination from the top, the saturated photocurrent increases at high biases, which is ascribed to the illumination-induced edge leakage current resulting from high electric field crowding at the contact periphery, or interface leakage current resulting from the traps and dislocations at the metal-semiconductor interface. It should be noted that with top illumination, the photogenerated carriers in the GaN cap layer can also contribute to the signal current, but this 7-nm-thick layer is so thin that its contribution can be neglected.

In order to confirm the charge variation under the dark and illuminated conditions, the *C-V* characteristics of the devices were measured at a frequency of 1 MHz. It can be seen from Fig. 2.3 that the measured capacitance initially increases with increasing bias voltage, because the depletion region of the anode contact shrinks. As bias further increases, most of the applied bias falls on the cathode contact and the capacitance starts to be dominated by the cathode depletion region. At even higher biases, the enlarging depletion region of the

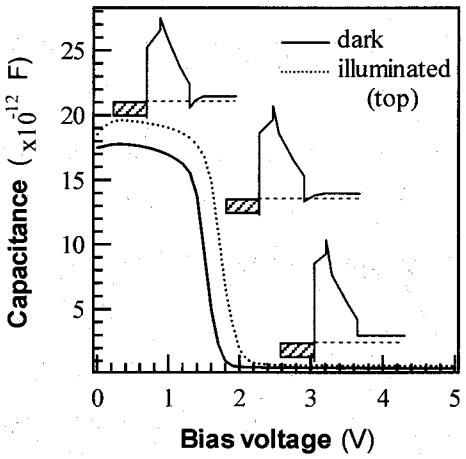

FIG. 2.3. C-V characteristics of the the AlGaN/GaN heterostructure MSM-PD under dark and illuminated (λ=365 nm) conditions. Schematic conduction band diagrams at cathode side for each constant capacitance region are also shown.

cathode contact results in a sharp decrease of the capacitance. The observed sharp decrease of the capacitance comes from the fact that the cathode depletion region starts to penetrate the 2DEG and extends into the GaN layer, i.e., the 2DEG channel below the cathode contact starts to be pinched off. After the pinch-off, the 2DEG under the cathode side is depleted as a consequence of the flat-band condition at the AlGaN/GaN heterointerface. This behavior is the same as the charge control in the HEMT device. Under the dark condition, the bias voltage required to achieve the pinch-off at the cathode side (V_{bpo}) is ~ 1.9 V. In the region $V_b > V_{bpo}$, the capacitance of the device is dominated by the depletion region at the cathode side and thus is due primarily to the background donors in the GaN channel layer as the 2DEG channel is depleted at this side. In the region $V_b < V_{bpo}$, the capacitance is due primarily to the carriers in the 2DEG channel.[8] In the presence of UV irradiation (λ=365 nm), the measured capacitance increases at a constant bias voltage smaller than V_{bpo}. This reflects that the illumination results in an increase in the 2DEG density because of the generation of photoelectrons in the GaN channel layer, leading to a shift of the *C-V* curve towards a larger value of V_{bpo}.[9]

Figure 2.4 shows the device spectral responsivity measured under 10 μW/cm^2 illumination. A sharp cutoff around the absorption band edge of GaN is found for both top and back illumination. With top illumination, UV-visible rejection of more than three orders of magnitude by λ=400 nm is obtained. At 15 V bias, a peak responsivity of 114 mA/W is demonstrated

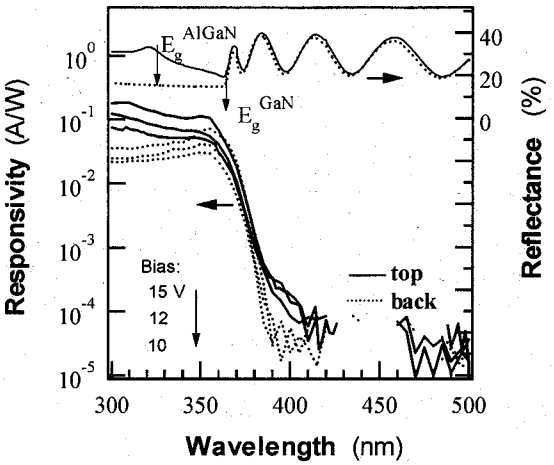

FIG. 2.4. Responsivities of the AlGaN/GaN heterostructure MSM-PD biased at 15, 12, and 10 V. The reflectance spectra of the heterostructure are also shown to identify the absorption band edges of AlGaN and GaN.

at 350 nm, corresponding to an external quantum efficiency (QE) of 40%. This value is comparable to those of the GaN-based normal MSM-PDs reported by Carrano *et al.* (QE~50%) [10] and *p-i-n* photodiodes reported by Collins *et al.* (QE~38%).[11] Although the back illumination may eliminate the loss by the electrodes and the AlGaN layer, the photoresponse (67 mA/W at 15 V bias) is smaller compared with the case of top illumination. This is because with back illumination, the *e-h* pairs that are created in the neutral region near the sapphire/GaN interface diffuse towards the depletion region near the AlGaN/GaN interface where they are separated and collected. Since the absorption depth in the GaN layer is typically less than 100 nm in this case, the photogenerated *e-h* pairs are far from the depletion region and suffer from recombination loss. A thinner GaN channel layer is expected to improve the responsivity with back illumination, but at the cost of degradation of the AlGaN/GaN interface.

Figure 2.4 also shows the photoresponse arising from the AlGaN layer when the device is illuminated from the top. For $\lambda<325$ nm, light is increasingly absorbed in the AlGaN layer as the photon energy increases and the responsivity becomes higher than that for $\lambda>325$ nm, since most of the photocarriers need not surmount the AlGaN/GaN discontinuity to be collected. This coincides with the result of our reflection measurement, which shows the absorption band edge of the AlGaN layer to be around 325 nm (Fig. 2.4).[12] Under this condition, the photocurrent relies on emission processes from either the Schottky or the 2DEG channel. Unlike the top illumination, the UV light irradiated from the back will be completely absorbed by the 0.8 μm GaN layer and, therefore, there is no photoresponse generated from the AlGaN layer in the case of back illumination.

In this research, MSM-PDs based on the undoped AlGaN/GaN HEMT structure operating in the visible blind region were fabricated. Dark-current density as low as 1.8×10^{-8} A/cm^2 at 10 V bias was obtained in these heterostructural MSM-PDs. A peak responsivity of 114 mA/W (QE=40%) was measured at 350 nm with top illumination, which is comparable to those of the superior GaN-based normal MSM-PDs and *p-i-n* photodiodes. The devices fabricated in this structure provide the possibility of combining light detection, signal amplification and processing into a single structure.

2.3 Barrier-height-enhanced *n*-GaN Schottky photodiodes using a thin *p*-GaN surface layer

GaN-AlGaN-based photodetectors have been the subject of intense research because of their potential applications in UV detection [13-16]. Among all types of UV photodetectors, Schottky photodiodes (PDs) are very attractive because of their simple material structure and fabrication process. In a Schottky PD, the photogenerated carriers are collected by the built-in electric field existing in a depletion region right at the semiconductor surface, and the transport of photocurrent is due to the majority charge carriers. It appears, therefore, that the Schottky PDs are advantageous in short-wavelength responsivity and response speed. For achieving low noise and high detectivity in a Schottky PD, however, low leakage current is required; the latter relatively high in Schottky PDs because of the charge injection originating from thermionic emission or the thermionic field-emission process. In fact, some efforts have been devoted to the suppression of leakage current in GaN-based Schottky barrier PDs. It has been suggested that preparing a SiO_2 surface-passivation layer or a low-temperature GaN cap layer on the surface of the *n*-GaN active layer can reduce the leakage current significantly [17-19]. An alternative approach which has been successfully applied to Si- and GaAs-based Schottky diodes is to prepare an oppositely doped surface layer to enhance the Schottky barrier height (SBH) and consequently reduce the leakage current [20-21]. In such a structure, band bending due to the space charge in the oppositely doped surface layer can result in an increase in the effective SBH to majority carriers, assuming that the doping density and thickness of the surface layer are designed so that the surface layer is fully depleted at thermal equilibrium. In this work, we demonstrate that by using a heavily doped *p*-GaN (p^+-GaN) surface layer, the barrier height of *n*-GaN Schottky PDs is increased from 1.09 eV to 1.16 eV and the leakage current density in the reverse-bias region of 0 to 5 V is reduced by about three orders of magnitude.

A 30- nm-thick GaN buffer layer was first deposited followed by a 1.5-μm-thick lightly Si-doped (n~8×10^{16} cm^{-3}) GaN layer. A 15-Å-thick heavily Mg-doped GaN layer (p~$1\text{-}2\times10^{18}$ cm^{-3}) was grown on the *n*-GaN layerto form the p^+/n-GaN structure. For the fabrication process, the ohmic contact regions were etched down to the *n*-GaN layer using the reactive ion etching (RIE) process employing BCl_3 gas. Then the Mg acceptor atoms

were activated using rapid thermal annealing (RTA) at 850 °C in the N_2 ambient for 30 min. Prior to the metal contact evaporation, the wafers were etched in boiling aqua regia and rinsed in deionized water to remove native oxide from the surface. Ti/Al/Ni/Au metallization was deposited on the *n*-GaN and annealed at 750 °C in the N_2 ambient for 30 s to obtain ohmic contacts. Transparent Pt film (85 Å) was next deposited on the p^+-GaN layer to provide Schottky contacts. Finally, a Ni/Au (200/2000 Å) bilayer was deposited as contact pads. For comparison, Schottky PDs based on the *n*-GaN without the p^+ layer with the same Si doping density (normal Schottky PDs) were also prepared with the same metallization procedure. Detector diameters are 390 μm for the Pt/p^+/*n*-GaN structure and 400 μm for the Pt/*n*-GaN structure.

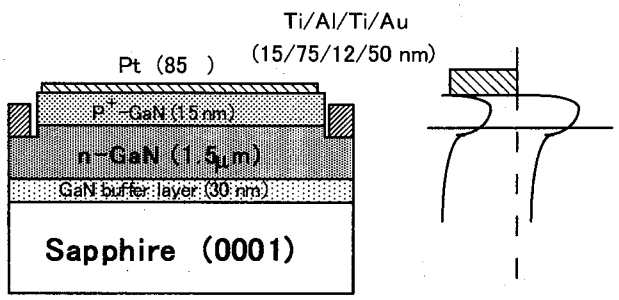

FIG. 2.5. (a) Schematic diagram of *n*-GaN Schottky PDs with p^+-GaN layer and (b) energy band diagram, in which x_m is the position of the potential maximum.

Figures 2.5(a) and 2.5(b) show, respectively, the schematic drawing of the Schottky PD with the p^+-GaN surface layer and a typical energy band diagram.

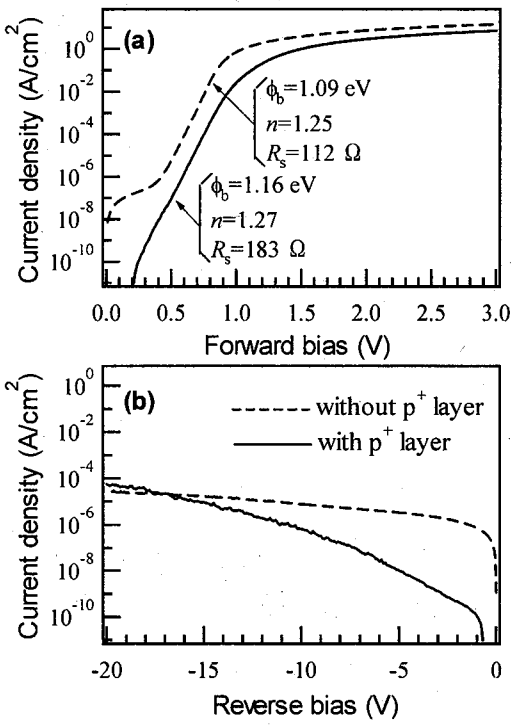

FIG. 2.6. (a) Forward and (b) reverse dark *I-V* characteristics of the *n*-GaN Schottky PDs with and without a 15 nm p^+ surface layer.

Dark *I-V* characteristics of the typical *n*-GaN Schottky PDs with and without the p^+ layer are shown in Fig. 2.6. Three parameters of the Schottky contact, SBH φ_{bn}, ideality factor *n*, and series resistance R_s, were derived from the forward *I-V* characteristics by the method described in ref. 22. For the normal *n*-GaN Schottky PD, the value of SBH (φ_{bn}=1.09 eV) is in general agreement with that reported by Wang *et al* [23]. In the Pt/p^+/*n*–GaN Schottky barrier structures, negative space charge resulting from ionized acceptors in the thin p^+ layer increases the

barrier to electron thermionic emission (Fig. 2.6(a)), leading to an effective SBH value of 1.16 eV. The values of ideality factor are larger than 1.2, indicating that the current transport mechanisms, other than thermoionic emission, may play roles in the fabricated diodes. The increase in R_s in the Pt/p^+/n–GaN Schottky PD is ascribed either to the higher resistive p^+ layer or to the slightly larger spacing between the Schottky contact dot and ohmic contact ring, as compared with those of the normal n-GaN Schottky PD. The reverse dark current density at -2 V bias is 4.8×10^{-10} A/cm^2 for the Schottky PD with the p^+ layer and 1.4×10^{-6} A/cm^2 for the Schottky PD without the p^+ layer, which denotes the suppression of the leakage current density by more than three orders of magnitude. We ascribe this suppression to the enhancement in the SBH, leading to a reduced value of the reverse saturation current density. Another possible contribution to the reduction of the leakage current is the opposite electric field in the region of x=0~x_m, which may hinder the charge carrier transport across the Pt/p^+–GaN interface under the reverse bias. It is observed, however, that the leakage-current curve of the Pt/p^+/n–GaN structure has a larger slope and tends to exceed that of the structure without the p^+-layer at the high-reverse-bias region, as shown in Fig. 2.6 (b). This is speculated as being due either to the deep-level defect-assisted tunneling transport resulting from the heavily Mg-doped layer or to the weakened role of the above-mentioned opposite electric field under the high-reverse-bias condition.

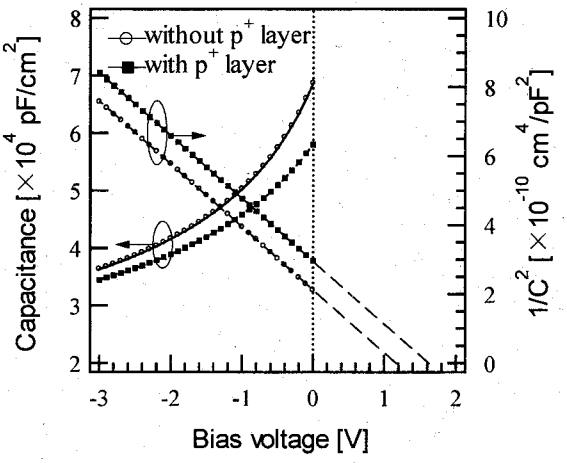

FIG. 2.7. *C-V* characteristics of the n-GaN Schottky PDs with and without a 15 nm p^+ surface layer.

Figure 2.7 shows the *C-V* characteristics of the two types of Schottky PDs. The relationship between the capacitance and the applied voltage in the metal/p^+/n Schottky structure can be described as [24]

$$\frac{A^2}{C^2}=\frac{2(V_{bi}-V-\frac{kT}{q})}{q\varepsilon_r\varepsilon_0 N_d}+K\cdot\frac{d^2}{(\varepsilon_r\varepsilon_0)^2} \qquad (1)$$

where A is the contact area, V_{bi} the built-in potential, V the applied voltage, d the thickness

of the p^+ surface layer, and ε_r the relative permittivity of the semiconductor. k, T, q, and ε_0 are as conventionally defined. The parameter $K=N_a/N_d$ is the compensation ratio, and in general, should be larger than unity. N_a and N_d are the donor and acceptor concentrations in the p^+ surface layer and n-layer, respectively. It should be noted that the first term in the eq. (1) is the same as the expression form for a normal Schottky diode, while the second term is a constant associated with the presence of the p^+ surface layer. The p^+ surface layer can be considered as an additional capacitor connected in series to the capacitor associated with the depletion region in the n-GaN layer. It is then easy to accept that the total capacitance is lower than that of a Schottky PD without the p^+ layer. The C-V measurements demonstrate that the zero-bias capacitances are 69 pF and 86 pF for the Schottky PD with and without the p^+ layer, respectively. According to eq. (1), the slope of the $(A/C)^2$-V plot, in the presence of the p^+ layer, will remain the same, while the intercept with the voltage axis will shift to higher forward voltages, as shown in Fig. 3. The increased intercept reflects an enhancement in the SBH; however, the effective SBH value can no longer be deduced from it directly. Unlike that obtained from the C-V measurement, the SBH obtained from the I-V measurement based on the transport of the majority carriers across the metal-semiconductor interface involves any of the potential barrier variation effects, and the effective SBH for the structure with the p^+ layer can be extracted directly in this manner [25].

For the normal Schottky PD, the value of the N_d evaluated from the slope of the $(A/C)^2$-V plot is 6.2×10^{16} cm^{-3}, which is comparable to that obtained from Hall measurement. The value of V_{bi} deduced from the intercept voltage is 1.27 V, corresponding to a SBH value of 1.36 eV. The difference between the SBH values evaluated from I-V and C-V measurements comes from the fact that, here, the thermionic emission is not the only mechanism by which electrons can cross the Schottky barrier. It has been proposed that in this case, a modified SBH named fundamental SBH, φ_{bf}, can be given by the following expression involving φ_{bn} and the n factor: [26]

$$\phi_{bf} = n\phi_{bn} - (n-1)\frac{kT}{q}\ln\frac{N_c}{N_d} \tag{2}$$

where N_c is the effective density states in the conduction band. From eq. (2), we obtained φ_{bf}=1.34 eV, which is consistent with the SBH value extracted by C-V measurement. By the second term in eq. (1), the value of N_a can be estimated as 1.6×10^{18} cm^{-3} from the vertical

intercept difference at zero bias between the two $(A/C)^2$-V plots. The enhancement of the SBH on n-type semiconductor by a thin p-type surface layer at zero bias is given by [24]

$$\Delta\phi_{bn} = \frac{V_{bi}\left[Kd - (W_{n0}^2 + Kd^2)^{1/2}\right]^2}{(K-1)W_{n0}^2} \tag{3}$$

and

$$W_{n0} = \left[2\varepsilon_r\varepsilon_0(V_{bi} - kT/q)/qN_d\right]^{1/2} \tag{4}$$

where W_{n0} is the zero-bias depletion width for the normal n-GaN Schottky contact. By using d=15 nm, N_d=6.2×10^{16} cm^{-3}, N_a=1.6×10^{18} cm^{-3}, V_{bi}=1.27 eV, we obtained a value of $\Delta\varphi_{bn}$=0.08 eV, which is in reasonable agreement with the value (0.07 eV) obtained from the I-V measurements.

Figure 2.8 shows the photoresponse spectra of the Schottky PDs with and without the SBH-enhanced p^+ layer biased at the low reverse voltages. All responses exhibited quite flat spectral responsivity above the absorption edge of GaN. In the case of the Schottky PD without the p^+ layer, the peak responsivity around 350 nm increased from 106 mA/W at zero bias to 121 mA/W at -2 V bias. The corresponding external QE values are 38% and 43%, respectively. For the Schottky PD with the p^+ layer, there exists a region between x=0 and x_m in which an opposite electric field tends to impede the collection of photogenerated carriers, as shown in Fig. 1(b). This causes a reduction of the UV responsivity in the SBH-enhanced Schottky PDs. The peak responsivity is only 58 mA/W at 350 nm under zero bias. With the reverse bias increasing, however, the photoresponse increases to 107 mA/W at -2 V bias, as a consequence of the broadening of the depleted region. An obvious advantage in the photoresponse characteristics to the SBH-enhanced GaN Schottky PD is the improvement in the visible rejection ratio. Improvement of more than one order of magnitude in the UV/visible rejection was achieved in the Schottky PD with the p^+-layer.

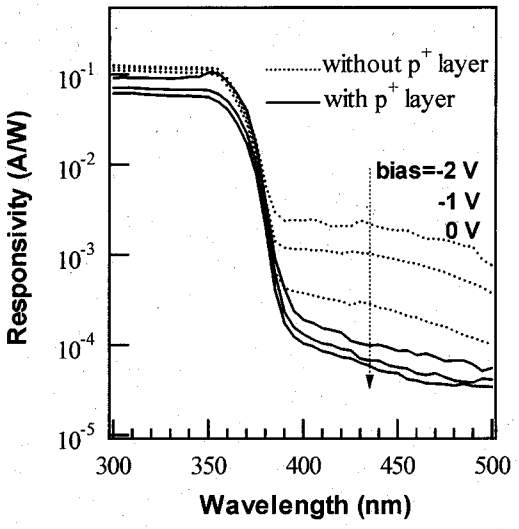

FIG. 2.8. Responsivities of the two types of GaN Schottky PDs biased at different voltages

In summary, a p^+-GaN surface layer of 15 nm was incorporated in *n*-GaN Schottky photodiode to enhance the effective Schottky barrier height. A barrier height of 1.09 eV for the normal *n*-GaN Schottky photodiode was increased to the effective barrier height of 1.16 eV. The resulting photodiodes show a reverse dark current density of as low as 4.8×10^{-10}A/cm^2 at –2V bias, which is about three orders of magnitude lower than that of the normal *n*-GaN Schottky photodiode. The lower dark current leads to a significant improvement in the visible rejection ratio. A peak responsivity of 107 mA/W was obtained at -2 V bias under the incident power density of 10 μW/cm^2, corresponding to an external quantum efficiency of 38%.

2.4 Low dark current achieved by using oxidized IrNi contact

The detection of UV radiation can be found its applications in missile plume detection, UV astronomy, flame sensors, engine and furnace control etc. and therefore has been studied quite extensively so far. Owing to their wide, direct bandgaps, superior radiation hardness and high temperature resistance, GaN based materials have been considered to be an excellent choice for the fabrication of high-performance UV photodetectors. In a variety of GaN-based photodetectors, Schottky photodiodes showed the advantages of high responsivity, high speed and simple fabrication [27, 28]. Compared with the *p-i-n* structure, another commonly used type of the photodiodes, the Schottky barrier structure is easier to fabricate since the *p* layer is no longer needed and so avoids the problems associated with the poor *p*-doping technology in GaN. The main issue in Schottky structure, however, arises essentially from the fact that the level of leakage current is higher than in *p-i-n* devices due to thermal stimulated currents. In order to reduce the leakage current, an effective method is to enhance the Schottky barrier height (SBH). Oxidized Ir/Ni bilayer was recently reported to form transparent ohmic contacts on *p*-GaN, in which the IrO_2 layer provides large work function while the NiO layer serves to prevent the outdiffusion of Ga and N atoms released from the decomposed GaN during annealing [29]. It is expected to use the oxidized IrNi layers to obtain Schottky contact with high SBH and high transparency on *n*-type GaN-based materials. In this work, the GaN Schottky photodiodes were fabricated using the oxidized IrNi layers as Schottky contacts.

The grown structure consists of a 30-nm-thick GaN nucleation layer at 500°C and a subsequent 3-μm-thick silicon doped n-GaN layer at 1180°C. Room temperature Hall-effect measurement showed the carrier density of 1.1×10^{17} cm^{-3} and electron mobility of 563.3 cm^2/Vs. Before the photolithography, the samples were dipped in boiling aqua regina for 10 min and followed by deionized water rinse as surface treatment. For the fabrication of the planar Schottky photodiodes, Ti/Al/Ni/Au (15/65/12/50 nm) ohmic contacts were deposited and annealed at 750 °C for 30s by RTA in N_2 ambient. Following the formation of ohmic contacts, Ir/Ni/Ir (40/40/40 Å) metallization was deposited to form Schottky contacts with diameter of 400 μ m. RTA of the Ir/Ni/Ir contacts was subsequently performed from 400 to 600 °C in O_2 ambient for 1 min. After the annealing, a Ni/Au bilayer was deposited as contact pads.

For dark *I-V* characteristics, it is found that with increasing the annealing temperature started from 400 °C, the SBH increases while the leakage current decreases. The maximum SBH and the minimum leakage current at –5 bias were determined for the 500 °C annealed samples. The resulting SBH is 1.28 eV, which is 0.33 eV higher than that of the as-deposited samples. At a bias of -5 V, the dark current density as low as 1.8×10^{-10} A/cm^2 was obtained, which is four orders of magnitude lower than the 3.7×10^{-6} A/cm^2 of the as-deposited samples as shown in Fig. 2.9. To our knowledge, this is the lowest value in the GaN based Schottky and *p-i-n* photodiodes. The greater than 1.2 ideality factors suggest that the transport mechanisms, other than the thermionic emission, are probably involved in these samples. A slight deterioration of the Schottky contacts was found after the 600 °C annealing. These results well coincide with those of Jang *et al.*, which indicate the optimum oxidization annealing for the Ir/Ni bilayer is achieved by 500 °C annealing in O_2 [29].

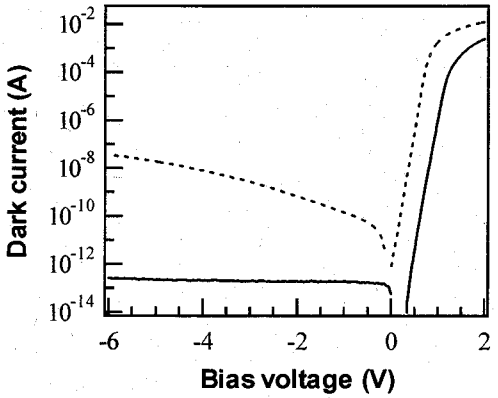

FIG. 2.9. Dark I-V characteristics of the Ir/Ni/Ir GaN Schottky photodiodes
····· as-deposited Schottky contact with SBH=0.95 eV, ideality factor (n)=1.30 and series resistance (R_s)=130 Ω
—— 500 °C annealed Schottky contact with SBH=1.28 eV, n=1.25 and R_s=526 Ω

Figure 2.10 shows the spectral responsivities of the Ir/Ni/Ir Schottky photodiodes biased at different voltages under an irradiant power density of 10 μW/cm^2. The sharp cutoff was observed at the band edge of GaN (36 nm). For 500 °C annealed photodiode, a more than three-orders of magnitude UV/visible rejection in responsivity by 400 nm is demonstrated for all bias conditions. The maximum responsivity for zero bias is 105 mA/W obtained at 345 nm, corresponding to an external QE of 38%. The external QE increases to 54% with the reverse bias increasing to15 V. Also shown for comparison is the responsivity of the as-deposited Ir/Ni/Ir Schottky photodiode with a maximum responsivity of 42 mA/W at the zero bias. The responsivity increases to 185 mA/W at -1 V bias, but at the cost of a poor visible rejection. The superior photoresponse of the Ir/Ni/Ir Schottky photodiode annealed at 500 °C in O_2 is ascribed to the enhanced SBH and transmittance of the Schottky contact. As shown in the inset of Fig. 2, the transmittance at 350 nm is 28.6% for the as-deposited contact and is enhanced to 62.9% for the 500 °C annealed contact. The enhanced SBH leads to a lower dark current and a lager depletion region, while the higher transmittance lets more irradiant flux to pass the Schottky contact.

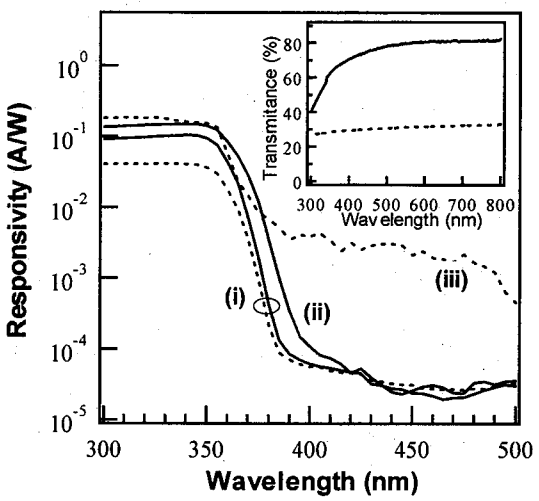

FIG. 2.10. Spectral response characteristics of the Ir/Ni/Ir GaN Schottky photodiodes. Inset: Transmittance of the Ir/Ni/Ir layes
..... as-deposited
——— 500 °C annealed in O_2
(i) zero bias; (ii) -1 V bias; (iii) -15 V bias.

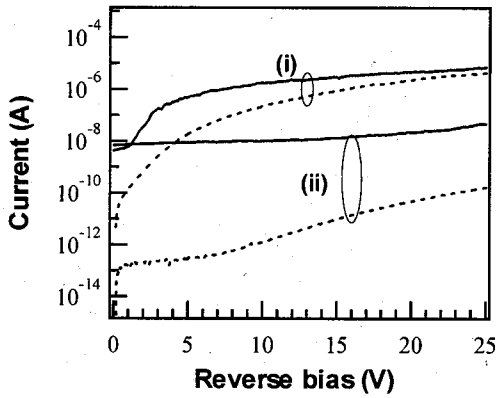

FIG. 2.11. Dark and illuminated reverse I-V curves of the Ir/Ni/Ir GaN Schottky photodiodes
..... dark current ——— photocurrent
(i) as-deposited ; (ii) 500 °C annealed in O_2

Photocurrent-voltage characteristics are depicted in Fig. 2.11. The irradiation wavelength is 350 nm with a power density of 50 μW/cm^2. For the photodiode with oxidized Schottky contact, there is a strong and relatively flat UV photoresponse below 15 V reverse

bias. The flat photocurrent is indicative of negligible photoconductive gain which usually adds noise to signal. While in the as-deposited Ir/Ni/Ir Schottky photodiode, the photoconductive gain mechanism dominates the photocurrent respose.

In many practical applications the Schottky photodiode is operated at zero bias. A figure of merit for the Schottky photodiodes is the R_0A product, where R_0 is the dynamic resistance at zero bias and can be expressed as [30],

$$R_0 = \left.\frac{dV_a}{dI}\right|_{V_a=0} = \frac{nkT}{qI_s} + R_s .$$

Assumed that the UV Schottky photodiode is thermal noise limited, the normalized detectivity (D^*) may be estimated as [31]

$$D^* = \Re_\lambda \left(\frac{R_0 A}{4kT}\right)^{1/2}$$

where R_λ is the device responsivity at zero bias. Since the detectivity D^* is proportional to $(R_0A)^{1/2}$ in the thermal-noise-limited case, a low reverse saturation current I_s (i.e., a high Schottky barrier height, ϕ_B) is necessary for the photodiode to achieve a large detectivity D*. With a responsivity value of 105 mA/W at 345 nm and a R_0A product of 4.7×10^{13} Ωcm^2, the zero-bias detectivity of the photodiode with oxidized Ir/Ni/Ir Schottky contact is estimated as 5.8×10^{15} cm $Hz^{1/2}W^{-1}$. This is one of the largest D* values ever obtained for GaN based photodiodes.

In summary, Ir/Ni/Ir metallization was employed as Schottky contacts of GaN Schottky photodiodes. After annealing at 500 °C in O_2 for 1 min, the Schottky contact achieved the maximum barrier height of 1.28 eV and the minimum dark current densities of 1.8×10^{-10} A/cm^2 at -5 V bias. The peak responsivity is 105 mA/W at zero bias and increases to150 mA/W at –15 V bias. The detectivity was estimated as 5.8×10^{15} $cmHz^{1/2}W^{-1}$ at zero bias. The superior performance of the Schottky photodiode is ascribed to the enhanced SBH and UV transparency of the oxidized IrNi Schottky contacts.

References

1. T. Egawa, H. Ishikawa, M. Umeno and T. Jimbo: Appl. Phys. Lett. **76** (2000) 121.
2. V. V. Kuryatkov, H. Temkin, J. C. Campbell and R. D. Dupuis: Appl. Phys. Lett. **78** (2001) 3340.
3. M. A. Khan, M. S. Shur, Q. Chen, J. N. Kuznia and C. J. Sun: Electron. Lett. **31** (1995) 398.
4. O. Ambacher, B. Foutz, J. Smart, J. R. Shealy, N. G. Weimann, K. Chu, M. Murphy, A. J. Sierakowski, W. J. Schaff, L. F. Eastman, R. Dimitrov, A. Mitchell and M. Stutzmann: J. Appl. Phys. **87** (2000) 334.
5. L. F. Eastman, V. Tilak, J. Smart, B. Green, E. M. Chumbes, R. Dimitrov, H. T. Kim, O. Ambacher, N. Weimann, T. Prunty, M. Murphy, W. Schaff and J. R. Shealy: IEEE Transaction on Electron Devices **48** (2001) 479.
6. E. T. Yu, X. Z. Dang, L. S. Yu, D. Qiao, P. M. Asbeck, S. S. Lau, G. J. Sullivan, K. S. Boutros and J. M. Redwing: Appl. Phys. Lett. **73** (1998) 1880.
7. E. J. Miller, X. Z. Dang, and E. T. Yu: J. Appl. Phys. **88** (2000) 5951.
8. S. Imanaga and H. Kawai: Jpn. J. Appl. Phys. **37** (1998) 5906.
9. F. Stengel, S. N. Mohammad and H. Morkoç: J. Appl. Phys. **80** (1996) 3031.
10. J. C. Carrano, T. Li, P. A. Grudowski, C. J. Eiting, R. D. Dupuis and J. C. Campbell: J. Appl. Phys. **83** (1998) 6148.
11. C. J. Collins, T. Li, A. L. Beck, R. D. Dupuis, J. C. Campbell, J. C. Carrano, M. J. Schurman and I. A. Ferguson: Appl. Phys. Lett. **75** (1999) 2138.
12. H. Jiang, G. Y. Zhao, H. Ishikawa, T. Egawa, T. Jimbo and M. Umeno: J. Appl. Phys. **89** (2001) 1046.
13. M. Razeghi and A. Rogalski: J. Appl. Phys. **79** (1996) 7433.
14. E. Monroy, F. Calle, J.L. Pau, F.J. Sánchez, E. Muñoz, F. Omnès, B. Beaumont and P. Gibart: J. Appl. Phys. **88** (2000) 2081.
15. J. C. Campbell, C. J. Collins, M. M. Wong, U. Chowdhury, A. L. Beck and R. D. Dupuis: Phys. Status Solidi A **188** (2001) 283;
16. T. Li, D. J. H. Lambert, M. M. Wong, C. J. Collins, B. Yang, A. L. Beck, U. Chowdhury, R. D. Dupuis and J. C. Campbell: IEEE J. Quantum Electron. **37** (2001) 538.

17. V. Adivarahan, G. Simin, J. W. Yang, A. Lunev, M. Asif Khan, N. Pala, M. Shur and R. Gaska: Appl. Phys. Lett. **77** (2000) 863.
18. E. Monroy, F. Calle, J. L. Pau, E. Muñoz and F. Omnès: Electron. Lett. **36** (2000) 2096.
19. M. L. Lee, J. K. Sheu, W. C. Lai, S. J. Chang, Y. K. Su, M. G. Chen, C. J. Kao, G. C. Chi and J. M. Tsai: Appl. Phys. Lett. **82** (2003) 2913.
20. J. M. Shannon: Solid-State Electron.**19** (1976) 537.
21. S. J. Eglash, N. Newman, S. Pan, D. Mo, K. Shenai, W. E. Spicer, F. A. Ponce and D. M. Collins: J. Appl. Phys. **61** (1987) 5159.
22. S. K. Cheung and N. W. Cheung: Appl. Phys. Lett. **49** (1986) 85.
23. L. Wang, M. I. Nathan, T-H. Lim, M. A. Khan and Q. Chen: Appl. Phys. Lett. **68** (1996) 1267.
24. G. Lubberts, B. C. Burkey, H. K. Bücher and E. L. Wolf: J. Appl. Phys. **45** (1974) 2180.
25. S. V. Averin, A. Kohl, R. Müller, J. Wisser and K. Heime: Solid-State Electron. **36** (1993) 61.
26. L. F. Wagner, R. W. Young and A. Sugerman: IEEE Electron Device Lett. **ED-4** (1983) 320.
27. Chen, Q., Yang, J. W., Osinsky, A., Gangopadhyay, S., Lim, B., Anwar, M. Z., Khan, M. A., Kuksenkov, D. and Temkin, H.: Appl. Phys. Lett. **70** (1997) 2277.
28. Biyikli, N., Kartaloglu, T., Aytur, O., Kimukin, I. and Ozbay, E.: Appl. Phys. Lett. **79** (2001) 2838.
29. Jang, H. W. and Lee, J. L.: J. Appl. Phys.**93** (2003) 5416.
30. Brutscher, N. and Hoheisel, M.: Solid-State Electron.**31** (1988) 87.
31. Collins, C. J., Li, T., Lambert, D. J. H., Wong, M. M., Dupuis, R. D. and Campbell, J. C.: Appl. Phys. Lett.**77** (2000) 2810.

3. $Al_{0.23}Ga_{0.77}N$ UVB Schottky photodiodes as flame sensor

--optimization for crystal growth and device processing

3.1 Epitaxial growth and experimental procedure

In this research phase, AlN/sapphire templates were started to be used as substrates. In order to suppress the gas phase parasitic reactions between TMA and NH_3, *low pressure* (LP) MOCVD method was used to deposit the $Al_xGa_{1-x}N$ (x>0.2) epitaxial layers for constructing UVB photodiode. The growth pressure was set at 100 torr. The MO source and growth temperature were same as those in the first phase.

For analyzing the structural properties of the AlGaN epitaxial layers, high resolution X-ray diffraction (HRXRD) technique using a Philips X'Pert PRO X-ray Diffraction System was employed. The instruments for *I-V* and *C-V* measurements are still those used before. New instrument was utilized to record the spectral photoresponses. The measurements were performed by using a light source comprising a quartz halogen lamp, a xenon-arc lamp and a deuterium (D2) lamp, a monochromator equipped with a 600 lines/mm ruled grating, and a Kethley 6517A programmable electrometer. The optical system is calibrated by a UV enhanced Si detector. Because of the attachment of D2 lamp, the wavelength of spectral responsivity can be measured from 200 nm to 600 nm.

3.2 Reduction of threading dislocations in AlGaN layers using high-temperature GaN interlayer

III-nitride optoelectronic devices operating in the UV spectral ranges of UVB (280-315 nm) and UVC (100-280 nm) are now the focus of intense research interest [1-3]. For the fabrication of these devices, thick $Al_xGa_{1-x}N$ epitaxial layers with high Al composition (x>0.20) and high-crystalline quality are essential. A major obstacle concerning the growth of such AlGaN layers is the large mismatches in the lattice constants and thermal expansion coefficients between the AlGaN and the commonly used substrate of sapphire. It is found that the thick $Al_xGa_{1-x}N$ (x>0.2) layers grown on sapphire substrate usually contain cracks and/or high densities of threading dislocations (TDs), even with the use of nucleation layers

(see Fig. 3.1). Such problem is also found in the AlGaN grown on GaN/sapphire template. To overcome this issue, many efforts have been done to accommodate the mismatches, and crack-free AlGaN layers with reduced TD density have been demonstrated by introducing low-temperature (LT) AlN interlayers [4] or AlN/AlGaN superlattices [5].

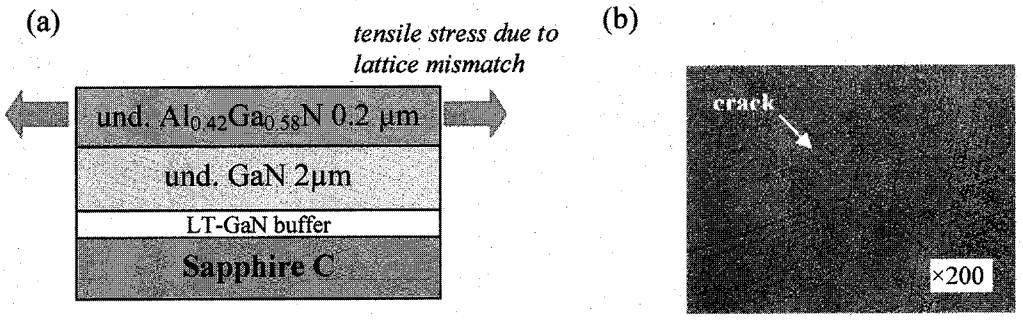

FIG. 3.1. (a) schematic structure of the 0.2-m-thick $Al_{42}Ga_{58}N$ layer grown on GaN/sapphire structure with LT-GaN nucleation layer in our lab. (b) photograph of the $Al_{42}Ga_{58}N$ layer shows a large number of cracks due to the tensile stress resulting from the lattice and thermal mismatch between AlGaN and GaN.

The recent success in the growth of thick AlN film on c-plane sapphire, the so-called AlN/sapphire template, provides a more encouraging solution to achieve high-crystalline quality $Al_xGa_{1-x}N$ ($x>0.2$) layers [3, 6]. Due to their much better lattice- and thermal-expansion matching, the AlGaN layers grown on the AlN/sapphire templates are easy to be free of cracks. One problem, however, appears to be the high number of edge TDs propagating from the underlying AlN layer [7]. Since the nucleation energy of the edge TDs is much smaller than that of the screw TDs, the major TDs existing in GaN-based film grown on c-plane sapphire are, in general, of edge type [8]. This is also the case for the AlGaN layers on AlN/sapphire templates. It is then of interest to reduce the edge TDs in the AlGaN layer. In this work, we demonstrate that the edge-type TD density can be efficiently suppressed by inserting a thin high-temperature (HT) GaN layer between the AlGaN layer and AlN/sapphire template. The effects of HT-GaN interlayer on the structural properties of AlGaN layer are also discussed.

The $Al_xGa_{1-x}N$ layers with Al composition of $x=0.23$ were grown by LP-MOCVD on 1-μm-thick AlN templates prepared by LP-MOCVD on sapphire C substrates. The growth on AlN/sapphire structure was initiated with a thin HT-GaN layer with thicknesses of 0, 20,

25 and 28 nm, respectively. Then, a 1.0-μm-thick Si doped $Al_{0.23}Ga_{0.77}N$ layer was grown with a SiH_4 flow rate of 2 sccm, followed by a 0.5-μm-thick undoped $Al_{0.23}Ga_{0.77}N$ layer. Both the growth processes of GaN and $Al_{0.23}Ga_{0.77}N$ were carried out at 1180 °C with a reactor pressure of 100 Torr. The V/III ratios for the growth of GaN and AlGaN are 3200 and 4000 respectively.

The structural properties of the samples were characterized by HRXRD. For the less perfect crystals, such as AlGaN layers grown on c-plane sapphire, the broadening of XRD peaks is dominated by three factors, namely, mosaicity, grain size and microstrain. The mosaicity is a measure of the grain misorientation described in terms of out-of-plane tilt and in-plane twist angles. As for the (0001) oriented AlGaN layer, the tilt misorientation is mainly related to the screw (***c***-type) threading dislocations (TDs) with Burgers vector $\boldsymbol{b}_c$ = [0001], while the twist is mainly associated with the edge (***a***-type) TDs with $\boldsymbol{b}_a$ =1/3[11$\bar{2}$0]. Assuming the screw TDs distributed at random, the density of screw TDs (ρ_c) can be estimated as $\rho_c = \alpha_\omega^2 / (4.35|\vec{b}_c|^2)$, where α_ω is the tilt angle. The edge TDs, however, are usually considered to distribute at grain boundaries separated with an average in-plane correlation length (L_a corresponds to average grain size), and the edge-TD density (ρ_a) can be assessed by a modified expression $\rho_a = \alpha_\phi / (2.1|\vec{b}_a|L_a)$, where α_ϕ is the twist angle [9].

To evaluate the mosaicity and TD density, rocking scans (ω scans) of symmetric (000*l*) (*l*=2, 4, and 6) and asymmetric (12$\bar{3}$1) reflections as well as an azimuthal scan (ϕ scan) of (12$\bar{3}$1) reflection were performed. The measured symmetric rocking curves were used to construct the Williamson-Hall (WH) plot of ($\beta_\omega \sin\theta/\lambda$) verse ($\sin\theta/\lambda$), where β_ω is the integral breadth of a given (000*l*) diffraction peak at 2θ angle, θ the diffraction angle and λ the wavelength of the incident Cu *K*α1. Note that the employed rocking curves refer to those taken under the triple-axis configuration, in which the three-bounce Ge (022) analyzer crystal employed provides a small detector angular acceptance to rule out the microstrain effect on the peak broadening. From a linear fit to the WH plot, the value of α_ω is derived as the slope and the value of L_a is derived from the intercept of vertical axis (y_0) with

$L_a = 0.9/(2y_0)$ [9]. The twist angle, however, is determined by recording both the ω and ϕ scans of $(12\bar{3}1)$ reflection in skew geometry. As proposed in Ref. 10, the average value of the full width at half-maximums (FWHMs) of these two reflection peaks gives a figure of merit for the twist.

In Table 3.1, the microstructural parameters of the samples analyzed from the HRXRD measurements are summarized. It demonstrates that the tilt misorientation in AlGaN layer is somewhat increased when the HT-GaN interlayer is inserted. The most increase in the tilt angle is 111 arcsec, corresponding to a change of 1.5×10^8 cm^{-2} in the screw-TD density.

TABLE 3.1. Structural parameters deduced from the HRXRD data for the samples grown with the HT-GaN interlayers of different thickness (t_{GaN}).

t_{GaN} (nm)	α_ω (arcsec)	L_a (μm)	α_ϕ (degree)	ρ_c (cm^{-2})	ρ_a (cm^{-2})
0	263	0.38	0.321	1.4×10^8	4.6×10^9
20	374	1.70	0.217	2.8×10^8	7.1×10^8
25	274	1.95	0.181	1.5×10^8	5.1×10^8
28	365	1.02	0.231	2.7×10^8	1.7×10^9

A possible reason for this increase is the screw-component threading segments from the misfit dislocations (MDs) induced by the interlayer, as will be further discussed later. In contrast, the twist misalignment in the AlGaN layers is obviously improved by inserting HT-GaN interlayer. A minimum twist angle (α_ϕ =0.181°) is obtained when the interlayer thickness is 25 nm, which is 0.14° less than that for the sample without the interlayer. The most improvement in the average in-plane correlation length is also found at this interlayer thickness. As the results, the edge-TD density is effectively suppressed from 4.6×10^9 cm^{-2} down to 5.1×10^8 cm^{-2}.

To understand more about the effect of the HT-GaN interlayer on the structural properties of AlGaN layer, the reciprocal space maps (RSMs) were recorded around $(20\bar{2}4)$ reflection. Figure 1 shows the RSMs of AlGaN layers grown without and with a 25 nm HT-GaN interlayer. The fully relaxed and fully strained positions relative to the reciprocal lattice points (RLPs) of $Al_xGa_{1-x}N$ (x=0~1) are drawn, respectively, as incline and vertical dashed

lines. In the locating procedure, the strain free in-and out-plane lattice constants are taken to be 3.1892 and 5.1850 Å for GaN, and 3.1114 and 4.9792 Å for AlN [11], respectively. For the AlGaN layer directly grown on AlN/sapphire template, the positions of AlGaN RLPs, as compared with that of the fully relaxed RLP, indicate that the AlGaN layer is compressively strained due to the constraint effect of AlN layer. It appears from Fig. 3.2(a) that this compressive strain is partially relaxed through a progressive strain-relief process, in which the in-plane lattice parameter is gradually increased while the out-of-plane lattice parameter is gradually reduced. Since the RLPs of AlGaN layer is primarily elongated along the Q_x direction, it can be drawn that in this case the limited in-plane correlation length, rather than the mosacity, is the predominant factor for the broad scattering [12]. On the other hand, by the insertion of a 25-nm-thick GaN, the AlGaN layer is almost fully relaxed via a rapid strain-relief process [Fig. 3.2(b)]. This leads to a significant improvement in the elongation and also an increase in the in-plane correlation length (Table 3.1). A distinct feature of this structure is that the GaN interlayer does not start growing pseudomorphic to the underlying AlN layer, due to the relative large lattice mismatch (2.5%) between AlN and GaN. In this case, interfacial MDs tend to be introduced to accommodate the lattice mismatch. It thus turns out that, through the RSMs, the inserted HT-GaN layer plays a role not only in the reduction of edge TDs, but also in the relaxation of compressive strain.

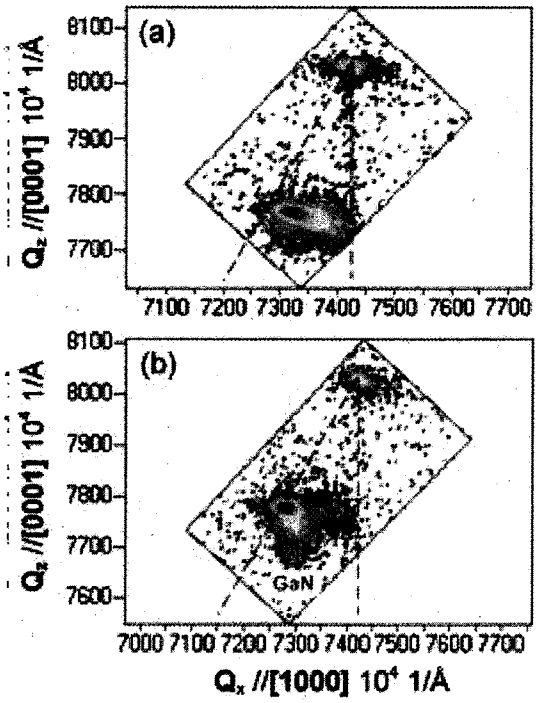

FIG. 3.2. Reciprocal space maps around ($20\bar{2}4$) reflections of the samples grown (a) without and (b) with a 25 nm HT-GaN interlayer.

A further investigation was performed by cross-sectional transmission electron microscopy (TEM) to get a direct view on the microstructures of the representative samples without and with a 25 nm HT-GaN interlayer. Under **g**=(0002) two-beam diffraction conditions, only the screw and mixed (*a*+*c* type) TDs with a *c*-type burgers vector

component are in contrast. As shown in Fig. 2(a) and (b), the TEM imagines reveal a low number of screw-component TDs in the AlGaN layers of the two samples. The estimated TD densities are ~1×10^8 cm^{-2} and ~2×10^8 cm^{-2} for the samples with and without a 25 nm HT-GaN layer respectively, which are consistent with the results from the HRXRD measurements. It is apparent that such low-TD densities in the AlGaN layers should benefit from the very few screw-component TDs running in the AlN layers.

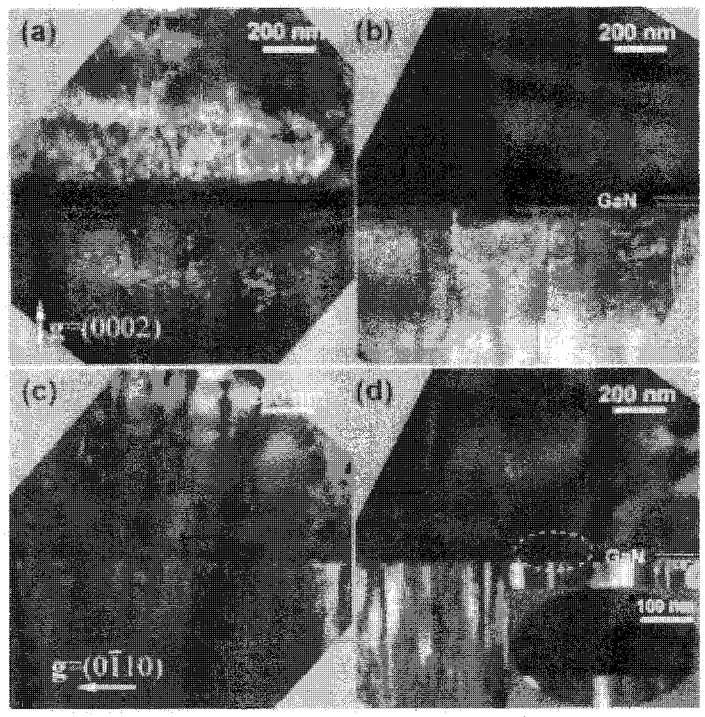

FIG. 3.3. Cross-sectional TEM images for the AlGaN layers grown on AlN/sapphire templates without [(a) and (c)] and with a 25 nm HT-GaN interlayer [(b) and (d)]. (a) and (b) are taken with the diffraction vector **g**= (0002) to image screw-component TDs; (c) and (d) with **g**= ($0\bar{1}10$) to image edge-component TDs. The inset of Fig. 3.3(d) is a magnified image of the dislocation loop marked in dashed circle.

In the Fig. 3.3(c) and (d), the TEM images taken in **g**=($0\bar{1}10$) two-beam diffraction conditions are shown, in which only the edge and mixed TDs with an ***a***-type burgers vector component are in contrast. A high number of edge TDs running along the growth direction can be observed in the underlying AlN layers. For the sample without the interlayer, these TDs run into the AlGaN layer and bend at the interface due to the compressive stress originating from the lattice mismatch between AlGaN and AlN. With the bending of line direction, some TDs meet and react, leading to a monotonic decrease in the edge-TD density.

The primary reactions of TD reduction are annihilation and fusion, whereas only the fusion, in which two TDs react to form a single TD, can be clearly observed in Fig. 3.3(c). After the reaction, many edge TDs are still left and their density is relatively high (~6×10^9 cm^{-2} estimated by TEM).

With the HT-GaN interlayer, the reduction of the edge TDs operates in a more efficient way. In Fig. 3.3(d), it can be seen that most of the edge TDs propagating from the underlying AlN layer are blocked by the interlayer, leading to a significant drop of the TD density in the subsequent AlGaN layer. The major reduction occurs by the bending and closing of pairs of TDs to form dislocation loops in the near-interlayer region. The estimated TD density is ~ 8×10^8 cm^{-2}, reasonably consistent with that deduced from the HRXRD evaluation.

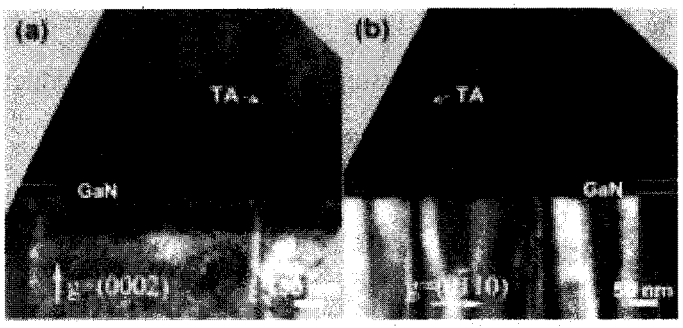

FIG. 3.4. Magnified TEM cross-sectional image for the sample grown with a-25 nm-thick HT-GaN interlayer under (a) bright-field **g**= (0002) and (b) dark-field **g**= ($0\bar{1}10$) diffraction conditions.

From the Fig. 3.3(b) and Fig. 3.4(a), it is clear that the HT-GaN interlayer can also block the screw-component TDs propagating from the AlN layer. An interesting observation in Fig.3.4 is a MD with its threading arm (TA). Since the threading segment is visible in either **g**= (0002) or **g**= ($0\bar{1}10$) image, its burgers vector should contain both ***a***- and ***c***-component, i.e., ***b***=***a***+***c***. Such a MD with its TA has been recently observed in the $Al_{0.22}Ga_{0.78}N$/GaN system which arises from the glide of dislocation half-loop on $\{11\bar{2}2\}$ plane [13]. While Fig. 3.4(b) indicates that here, the MD segment is generated at GaN/AlN interface, and moves into the AlGaN layer in form of TA. We speculate that the slight increases in the tilt misorientation after the insertion of HT-GaN interlayers may result from the screw components of such mixed-type TAs. As a mixed-TD is a combination of a screw

and an edge component, the mixed-TAs may also contribute to an increase in the twist angle which is, however, much less than the decrease due to the blocked edge-TDs.

In summary, the reduction of TD density in $Al_{0.23}Ga_{0.77}N$ layer grown on AlN/sapphire template has been realized by insertion of a HT-GaN interlayer. Structural parameters deduced from the HRXRD measurements show that the reduction of TD density is ascribed to the decrease of edge TDs, while the screw-TD density (or strictly speaking, screw-component TD density) is slightly increased. TEM observations evidence the HRXRD results and further reveal that such an interlayer can indeed block both the edge and screw TDs propagating from the AlN layer. The slight increase in the screw-TD density is speculated to result from the screw-component TAs of the MDs induced due to the interlayer. At an optimum interlayer thickness of 25 nm, the edge-TD density is reduced by one order of magnitude, while the screw-TD density is not much increased. It should be noted that due to the absorption of UVB and UVC light by the HT-GaN interlayer, a tradeoff is required between the light-transmission loss and the TD reduction in case of light extraction or illumination from the substrate backside.

3.3 AlGaN UVB Photodetectors fabricated on AlN/sapphire template

Recent progress in developing AlGaN based UV PDs has demonstrated their great potential as an alternative to the traditional UV sensing devices, such as PMTs and Si UV detectors, which are high cost, unstable or inefficiency [14-18]. AlGaN UVB photodetectors with the long-wavelength cutoff in the region of 280~320 nm are of interest for a variety of applications. Topics include ozone layer monitoring, medical and chemical analyses, combustion and flame detection, UV curing detection, phototherapy control, and personal exposure monitors etc [19]. A key issue limiting the performance of the state-of–art AlGaN UVB PDs is the cracks and/or high-density defects present in the AlGaN active epilayer, due to the lattice and thermal mismatch between the AlGaN and the underlying epilayer. The recent achievement of AlN($\geq$1 μm)/sapphire template is expected to improve this problem. In the section 3.2, we demonstrated that the threading dislocation density in the $Al_{0.23}Ga_{0.77}N$ layer grown on AlN templates can be reduced by inserting a thin HT-GaN interlayer. In this section, we describe the fabrication and characterization of the $Al_{0.23}Ga_{0.77}N$ UVB Schottky

photodiode based on AlN/sapphire template with and without HT-GaN interlayer.

The epitaxial structures of those grown on AlN templates has described in the section 3.2. Among the samples with different HT-GaN interlayer thicknesses, we selected the 25-nm thick one which shows the most reduction in dislocation density to be used for device fabrication. For the purpose of comparison, another set of $Al_{0.23}Ga_{0.77}N$ layer on GaN/sapphire structure was also grown on sapphire. The epitaxial structure includes a 30-nm-thick GaN buffer layer grown at 500 ℃, a subsequent 2 μm-thick i-GaN layer grown at atmosphere and 1180 ℃, and a 0.2 μm unintentionally doped $Al_{0.23}Ga_{0.77}N$ active layer grown at 120 torr and 1180 ℃. A thicker active layer is expected, but with the occurrence of cracks in our samples based on GaN/sapphire structure.

XRD measurements showed that the FWHMs of the (004) and (204) rocking curves are 362 and 789 arcsec for the $Al_{0.23}Ga_{0.77}N$ on GaN/sapphire, 225 and 857 arcsec for the $Al_{0.23}Ga_{0.77}N$ on AlN/sapphire template without HT-GaN interlayer, and 247 and 564 arcsec for the $Al_{0.23}Ga_{0.77}N$ on AlN/sapphire template with a 25-nm HT-GaN interlayer, respectively, indicating that the lowest TD density exists in the $Al_{0.23}Ga_{0.77}N$ layers deposited on AlN template with a HT-GaN interlayer.

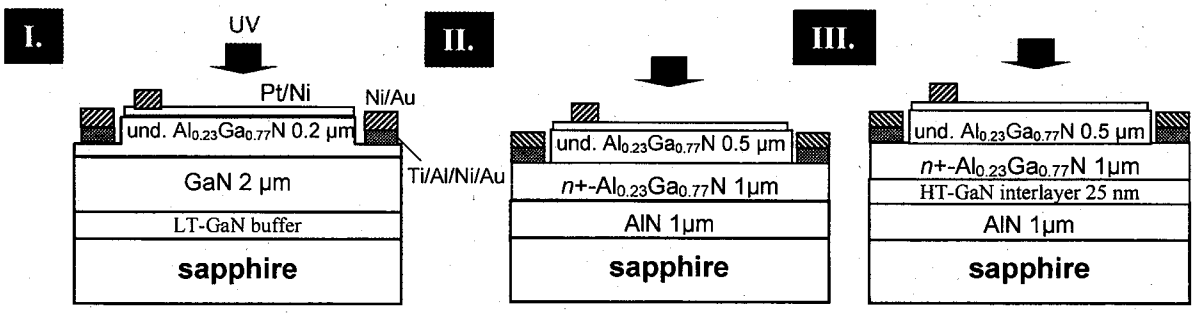

FIG. 3.5 Schematic cross-section of the UVB AlGaN Schottky photodiodes fabricated on (a) GaN/sapphire, (b) AlN/sapphire template, and (c) AlN/sapphire template with a 25-nm thick HT-GaN interlayer.

The schematic cross-section structures of the three devices were depicted in Fig. 3.5. Mesa structures were defined by RIE using BCl_3 gas. Ohmic contacts were formed with e-beam deposited Ti/Al/Ni/Au. The transparent Schottky-contact dots with a diameter of

400 μm were formed with Pt/Ni (70/15 Å) layers, which was deposited using e-beam evaporation and a standard lift-off process. Probe pads were deposited with Ni/Au bilayer.

Dark *I-V* characteristics of the resulting Schottky PDs were shown in Fig. 3.6. For the device fabricated on AlN/sapphire template with a 25-nm HT-GaN interlayer, the leakage current is only 2.4 pA at -5 V bias, corresponding to a current density of 3.3×10^{-10} A/cm^2. This value is about three orders lower than that of the $Al_{0.23}Ga_{0.77}N$ PDs fabricated on GaN/sapphire structure. A comparison of the dark current density at -5 V bias for the three samples with different structures are listed in Table 3.1. A comparison of the dark current density at -5 V bias for the three samples with different structures are listed in Table 3.2. The lowest leakage (dark) current density achieved in the sample with a HT-GaN interlayer is ascribed to the low defect density in the $Al_{0.23}Ga_{0.77}N$ layers. The dark current in the sample directly grown on AlN template is lower than that of the sample on GaN/sapphire, but is much higher as compared with that in the structure with interlayer. It has been pointed out that the screw-type TD is a primary source of the leakage current in GaN Schottky diode [20]. As shown in the Table 3.1, the estimation from XRD data shows, however, that the screw-type TD densities are very close in the two-type samples on AlN template with and without HT-GaN interlayer. The source for this relatively high leakage current is still not clear now. A possible reason is that the high-density edge-type TDs shown in the structure directly grown on AlN template also contribute to the leakage current.

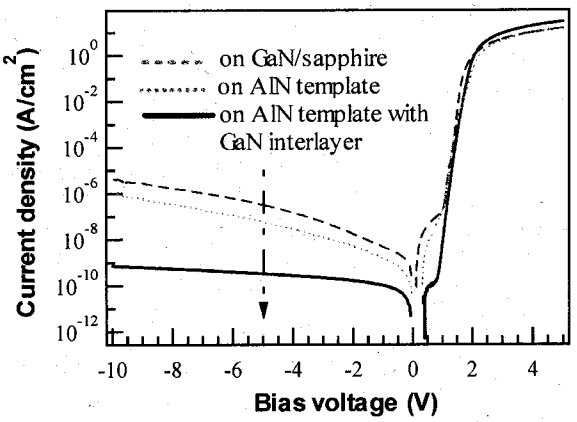

FIG. 3.6. Dark I-V characteristics of the $Al_{0.23}Ga_{0.77}N$ Schottky PDs fabricated on AlN/sapphire templates (with and without HT-GaN interlayer) and GaN /sapphire structure.

Spectral responses of the photodiodes were measured in the wavelength range of 500~200 nm. The photodiode with the HT–GaN interlayer structure exhibits a sharp cutoff at the band edge of $Al_{0.23}Ga_{0.77}N$ (~310 nm, as shown in Fig. 3.7). The rejection ratio is

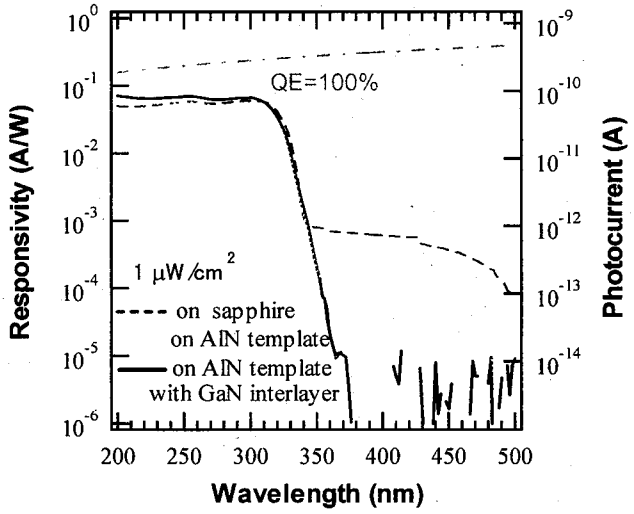

FIG. 3.7. Spectral responsivities of the zero-bias UVB Schottky PDs with the three different structures under the constant irradiation intensity of 1 μW/cm^2.

more than four orders of magnitude by λ=360 nm. At a bias of -5 V, the responsivity is 58.7 mA/W under an irradiation density of 1 μW/cm^2 with a wavelength of 310 nm, giving the external *QE* of 23.5%. For the photodiode constructed on GaN/sapphire structure, the band-edge cutoff wavelength and the peak responsivity are almost same as those of the photodiode on AlN template. The rejection ratio, however, is only two orders of magnitude by 360 nm. We speculate that the larger leakage current combined with the long-wavelength response arising from the *i*-GaN layer contribute to this lower rejection ratio. In the case of the photodiode directly grown on AlN template, the inferior rejection ratio is due mainly to the relatively high leakage current.

TABLE 3.2 Comparison for the performance parameters (dark current density at -5 V, J_d, responsivity, external QE, and rejection ratio by 360 nm) of the three different structure samples (I. grown on GaN/sapphire, II. grown on AlN template without interlayer, III. grown on AlN template with a 25-nm-thick HT-GaN interlayer).

Performance parameters	I.	II.	III.
dark current J_d @-5V (A/cm^2)	3.3×10^{-10}	3.3×10^{-10}	3.3×10^{-10}
responsivity (mA/W)	58.2	53.7	58.7
external *QE* (%)	23.3	21.2	23.5
rejection ratio by 360 nm (orders of magnitude)	2	3	4

As illustrated in Fig. 1.1, the luminescence spectrum of gas flame has a peak at 310 nm. According to this spectrum, the AlGaN UVB Schottky PDs should have response to the lighter flame due to the emission of UVB light. Since the light intensity of UVB is very weak, large area photodiode is expected to be used to get enhanced photoresponse. In the

meanwhile, low dark current is also demanded. A large size UVB Schottky photodiode with active area of 4×4 mm^2 was, therefore, fabricated on AlN template with a 25-nm HT GaN interlayer. A photograph of the resulting device is shown in Fig. 3.8(a). The photoresponses of our 4×4 mm^2 size UVB photodiode to the lighter flame are demonstrated in Fig. 3.8(c). Under the dark background, it can be seen that the UVB photodiode has clear photoresponses to the lighter flame. The background noise of room light was found, however, to result in responses about half as large as the lighter-flame signal. Therefore, to eliminate the effect of room light, it is needed to develop high-performance solar-blind (UVC) AlGaN photodiodes.

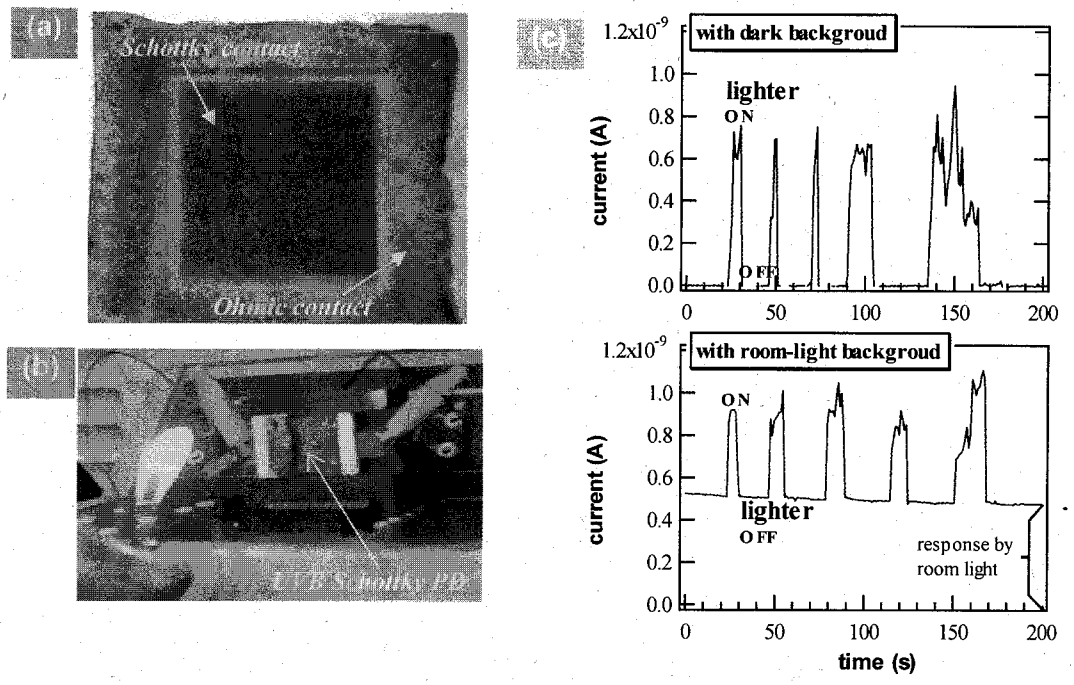

FIG. 3.8. (a) photograph of the UVB Schottky PD (4×4 mm^2 active area) fabricated on AlN template with the insertion of a 25-nm-thick HT-GaN interlayer. (b) photograph of the lighter flame detection apparatus. (c) photoresponses to lighter flame detected by the UVB Schottky PD biased at 0 V and placed ~15 cm apart in the backgrounds of dark and room light, respectively.

In this phase of our research project, we have achieved the high-performance $Al_{0.23}Ga_{0.77}N$ UVB Schottky-PDs based on AlN/sapphire template. With the reduction of TD density in the AlGaN layers by inserting a HT-GaN interlayer, the fabricated devices show the improved performances of low dark current and high UVA rejection ratio. Dark current density as low as 3.3×10^{-10} A/cm^2 at -5 V bias and zero-bias external QE of 23.5% at 310

nm were obtained. The capability for detecting the flame of lighter is demonstrated by the photodiode with the large active-area of 4×4 mm^2.

References

1. M. Razeghi, A. Yasan, R. McClintock, K. Mayes, D. Shiell, S. R. Darvish, P. Kung: Phys. Status Solidi C **1** (1999) S141.
2. H. Amano and I. Akasaki, Opt. Mater. **19**, 219 (2002).
3. J. P. Zhang, H. M. Wang, W. H. Sun, V. Adivarahan, S. Wu, A. Chitnis, C. Q. Chen, M. Shatalov, E. Kuokstis, J. W. Yang, M. A. Khan: J. Electron. Mater. **32** (2003) 364.
4. H. Amano, M. Iwaya, N. Hayashi, T. Kashima, S. Nitta, C. Wetzel, and I. Akasaki: Phys. Status Solidi B **216** (1999) 683.
5. J. P. Zhang, H. M. Wang, M. E. Gaevski, C. Q. Chen, Q. Fareed, J. W. Yang, G. Simin, M. Asif Khan: Appl. Phys. Lett. **80** (2002) 3542.
6. T. Shibata, K. Asai, S. Sumiya, M. Mouri, M. Tanaka, O. Oda, H. Katsukawa, H. Miyake, and K. Hiramatsu: Phys. Status Solidi C **0** (2003) 2023.
7. N. Kuwano, T. Tsuruda, Y. Kida, H. Miyake, K. Hiramatsu, T.Shibata: Phys. Status Solidi C**0** (2003) 2444.
8. L. Sugiura: J. Appl. Phys. **81** (1997) 1633.
9. T. Metzger, R. Höpler, E. Born, O. Ambacher, M. Stutzmann, R. Stömmer, M. Schuster, H. Göbel, S. Christiansen, M. Albrecht, and H. P. Strunk: Philos. Mag. A **77** (1998) 1013, and references cited therein.
10. X. H. Zheng, H. Chen, Z. B. Yan, Y. J. Han, H. B. Yu, D. S. Li, Q. Huang and J. M. Zhou: J. Cryst. Growth **255** (2003) 63.
11. H. Jiang, G. Y. Zhao, H. Isikawa, T. Egawa, T. Jimbo, and M. Umeno: J. Appl. Phys. **89** (2001) 1046.
12. R. Chierchia, T. Bottcher, S. Figge, M. Diesselberg, H. Heinke, and D. Hommel: Phys. Status Solidi B **228** (2001) 403.
13. J. A. Floro, D. M. Follstaedt, P. Provencio, S. J. Hearne, and S. R. Lee: J. Appl. Phys. **96** (2004) 7087.
14. J. C. Campbell, C. J. Collins, M. M. Wong, U. Chowdhury, A. L. Beck, and R. D. Dupuis: Phys. Stat. Sol. A. **188** (2001) 283.

15. C. J. Collins, U. Chowdhury, M. M. Wong, B. Yang, A. L. Beck, R. D. Dupuis, and J. C. Campbell: Electron. Lett. **38** (2002) 824.
16. N. Biyikli, O. Aytur, I. Kimukin, T. Tut, and E. Ozbay: Appl. Phys. Lett. **81** (2002) 3272.
17. C. Pernot, A. Hirano, M. Iwaya, T. Detchprohm, H. Amano and I. Akasaki: Jpn. J. Appl. Phys., **39** (2000) L387.
18. J. D. Brown, J. Matthews, S. Harney, J. C. Boney, J. F. Schetzina, J. D. Benson, K. V. Dang, T. Nohava, W. Yang, and S. Krishnankutty: MRS Internet J. Nitride Semicond. Res. **5S1** (2000) W1.9.
19. E. Muñoz, E. Monroy, J.L. Pau, F. Calle, F. Omnès, and P. Gibart: J. of Phys. : Cond. Matter. **13** (2001) 7115.
20. J. W. P. Hsu, M. J. Manfra, D. V. Lang, S. Richter, S. N. G. Chu, A. M. Sergent, R. N. Kleiman, L. N. Pfeiffer, and R. J. Molnar: Appl. Phys. Lett. **78** (2001)1685.

4. AlGaN solar-blind photodiodes

4.1 Epitaxial growth and experimental procedure

In this research phase, in order to fabricate solar-bind photodiodes, the growth of $Al_xGa_{1-x}N$ layers was shifted to high Al composition AlGaN with x>0.4. The growth method is still the LP-MOCVD operating at pressure of 100 torr.

For the deposition of Schottky photodiode structure, the growth temperature was kept at 1180 °C, while for the deposition of *p-i-n* photodiode structure, the temperature was adjusted to 1170 °C due to the upgrade of Taiyo Nippon Sanso SR2000 MOCVD system.

It has been realized that reducing the dislocations in the AlGaN epitaxial layers is very important for improving the photodiode performance in terms of dark current and rejection ratio. Accordingly, in this phase, our task is to grow low threading dislocation (TD) density AlGaN epitaxial films. The goal is to reduce the dislocation density to a level comparable to that of a common GaN layer grown on sapphire substrate (the total TD density of screw-type and edge-type is in the range of high 10^8 to low 10^9 cm^{-2}). To estimate the dislocation density, the method described in the section 3.2 can be used. It has been well established, however, in $Al_xGa_{1-x}N$ epitaxial films that the X-ray rocking curve for the symmetric (0002) reflection is broadened only by screw-component TDs, while the X-ray rocking curve for the asymmetric (10 $\bar{1}$ 2) reflection is broadened by all TDs [1]. The FWHM of ω scan thus reflects the epitaxial quality of the grown film. For simplification, we define a goal zone of the FWHMs for (0002) and (10 $\bar{1}$ 2) reflections (as shown in Fig. 4.1), in which the corresponding TD density in $Al_xGa_{1-x}N$ (x>0.4) layers is approximate to that in a general GaN layer grown on sapphire substrate.

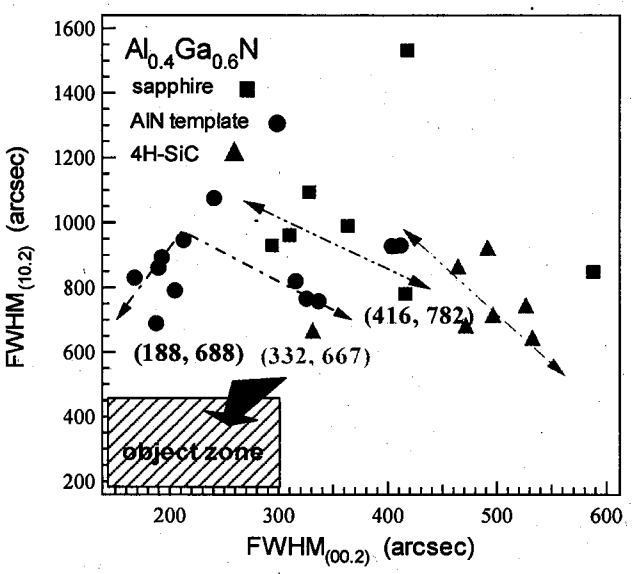

FIG. 4.1. FWHMs of the HRXRD rocking curves for the (0002) and (10 $\bar{1}$ 2) reflections of $Al_{0.4}Ga_{0.6}N$ films grown on substrates of sapphire, 4H-SiC, and AlN/sapphire template, respectively.

In an aim for comparison, we have grown the $Al_{0.4}Ga_{0.6}N$ epilayers on the substrates of sapphire, 4H-SiC, and AlN/spphire template, respectively. In the three series samples, the $Al_{0.4}Ga_{0.6}N$ epilayer grown on AlN template demonstrates the lowest TD density, suggesting that the AlN template may be the most proper substrate for fabricating solar-blind photodiodes. Besides, the experimental data from XRD measurements indicates that reducing the FWHM of (0002) [or $(10\bar{1}2)$] rocking curve always results in an increase in the FWHM of another reflection. That is, there is a trade off between the screw type and edge type TD density. Therefore, in this stage, our research on growth focused on providing an acceptable level of overall TD density.

For fabricating solar-blind photodiodes, the primary processing procedure is identical to that described in section 3.1. In the fabrication of *p-i-n* solar-blind photodiodes, *p*-type activation was performed by thermal annealing in N_2 ambient at 800 °C for 30 min.

4.2 AlGaN solar-blind Schottky photodiodes on 4H-SiC substrates

The development of AlGaN based UV photodetectors is driven by the requirement for the compact, stable, and low cost UV sensing device in both the military and industrial applications, such as early missile threat warning, secure space communications, and flame detection [2-5]. It is of special interest for the $Al_xGa_{1-x}N$ photodetectors with the Al composition of $x \geq 0.4$, which have a long-wavelength response cutoff around 280 nm. Since the solar radiation with wavelengths shorter than 280 nm is filtered out by the ozone layer, the $Al_xGa_{1-x}N$ ($x \geq 0.4$) photodetectors operating in this so-called solar-blind region are inherently able to detect low-intensity terrestrial UV signals with minimum natural background interference. Compared with photoconductors, photovoltaic detectors would be the better choice for many solar-blind applications due to their potential to provide low dark current, high UV/solar rejection and high detectivity at low operating bias. To date, solar-blind AlGaN Schottky and *p-i-n* photodiodes with low dark current, high quantum efficiency and high detectivity performance have been reported [6-11]. Despite these advances, the performance of state-of–art AlGaN solar-blind photodiodes is still limited by the high density of defects present in AlGaN epilayers. In general, AlGaN epilayers are grown on sapphire substrates. The large lattice and thermal expansion mismatches between

the sapphire and the subsequent epilayers often cause crack network and/or high-density threading dislocations (TDs) in AlGaN layers, even with the introduction of buffer layers. The high-density TDs, however, were found to be responsible for the low performance, such as large leakage (dark) current and broad spectral cutoff, of AlGaN based photovoltaic detectors [4], [12], [13].

Silicon carbide has a much better lattice match to AlN (1.1%) and GaN (3.5%), and is gaining increased popularity as a substrate for the growth of the $Al_xGa_{1-x}N$ epilayers. It is expected to grow high quality crack-free $Al_xGa_{1-x}N$ ($x \geq 0.4$) layers on SiC substrates to achieve high-performance solar-blind photodiodes. The AlGaN epitaxial layers for the Schottky-photodiode structure were grown on n-type $(0001)_{Si}$ 4H-SiC substrates LP-MOCVD at 100 torr. Before the growth, substrates were cleaned in organic solvents and etched in H_2SO_4:H_2O_2 (4:1) and dilute HF solutions and then rinsed in deionized water. Epitaxial growth started with the deposition of a 0.2-um AlN layer, followed by a 0.1-um thick graded layer and a 1 μm-thick unintentionally-doped $Al_{0.42}Ga_{0.58}N$ layer. A 1 μm-thick highly doped (n^+~1.8×10^{18} cm^{-3}) $Al_{0.42}Ga_{0.58}N$ layer was subsequently deposited to provide ohmic contact. Finally, a 0.5-μm thick, unintentionally-doped $Al_{0.42}Ga_{0.58}N$ was grown as

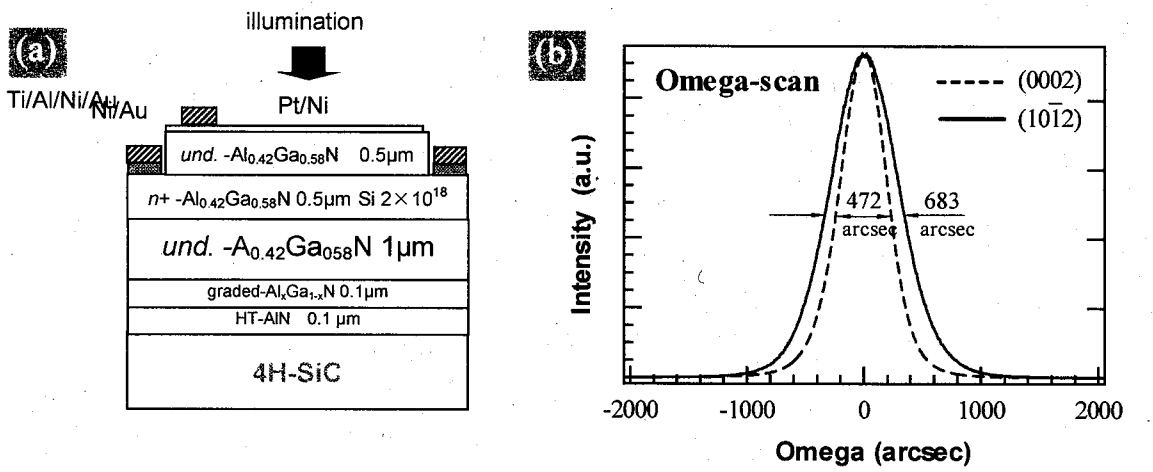

FIG. 4.2. (a) Cross-sectional schematic view of the solar-blind AlGaN Schottky photodiode based on n-type 4H-SiC substrate. (b)HRXRD rocking curves of the (0002) and (10 $\bar{1}$ 2) reflections from $Al_{0.4}Ga_{0.6}N$ films.

active layer. A mirror-like and crack-free surface morphology was observed for the grown sample. The structural properties of the $Al_{0.42}Ga_{0.58}N$ layers were investigated with HRXRD measurements. Figure 4.2 depicts the HRXRD rocking curves (ω scan) of the (0002) and

$(10\bar{1}2)$ diffractions. As shown in Fig. 1, the FWHM values of the (0002) and $(10\bar{1}2)$ diffraction peaks are 472 and 683 arcsec, respectively, indicating a high crystalline quality.

For fabrication process, the ohmic contact regions were etched down to the n^+-$Al_{0.42}Ga_{0.58}N$ layer using RIE process with 10 sccm BCl_3 at 3 Pa and 10 W RF power. Prior to the metal contact evaporation, the wafers were etched in boiling aqua regia and rinsed in deionized water to remove native oxide from the surface. Ohmic contacts were formed by electron-beam deposition of Ti/Al/Ni/Au (150/800/120/600 Å) and a lift-off process, followed by an 800 °C anneal for 30 sec in the N_2 ambient. Pt/Ni layers (60/20 Å) were deposited on the undoped AlGaN layer and lifted off to obtain rectifying contacts with an area of 1.0×1.0 mm^2. Ni/Au layers (200/2000 Å) were finally deposited as contact pads.

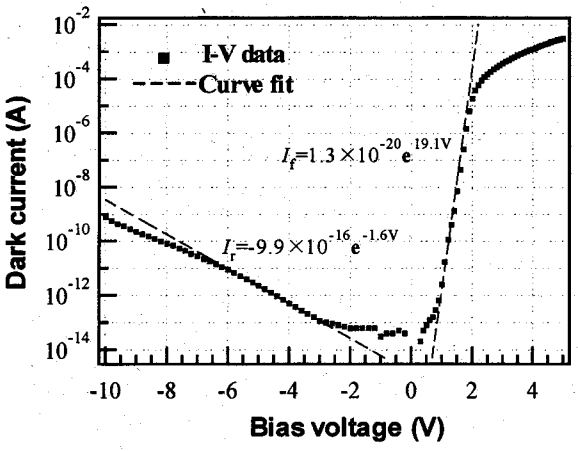

FIG. 4.3. Dark *I-V* characteristics of the solar-blind AlGaN Schottky PD with Schottky contact area of 1×1 mm2. The dash lines represent the exponential fits to the forward and reverse I-V curves.

Dark *I-V* characteristics of the fabricated AlGaN Schottky PDs were shown in Fig. 4.3. The figures of merit are: an ideality factor n=2.0, Schottky barrier height of φ_{bn} =1.4 eV, and a forward/reverse current ratio I_f/I_r=1.4×10^9 at +/-5 V. The value of ideality factor largely deviating from unity might be caused by the generation and recombination of carriers in the depletion region, interface states, and thermionic field emission in the fabricated diodes. The reverse dark current at a typical 5 V bias is 2.2 pA, corresponding to a current density of 2.2×10^{-10} A/cm^2. This value is one of the lowest values reported for AlGaN Schottky photodiodes. We ascribe this low leakage current to the high crystalline quality of AlGaN epilayers.

Using the method described in the Ref. 14, the dynamic resistance R_0, which is defined as $R_0 = (dI/dV)^{-1}|_{V=0}$, was extracted from the exponential curve fittings to both the forward and reverse dark I-V curves. The consequent value is R_0=6.4×10^{14}Ω, leading to the resistance-area product R_0A=6.4×10^{12} Ωcm^2.

Figure 4.4(a) shows the photocurrent spectra of the zero-bias Schottky photodiode

illuminated under the different irradiation power densities. Also shown is the photocurrent spectrum at -5 V bias with 1 μW/cm^2 illumination. The photocurrents were measured with the subtraction of the dark current. All responses exhibited a sharp cut-off around 280 nm. Under the low-intensity illumination of 10 nW/cm^2, rejection of more than two orders of magnitude was achieved in the wavelength range of 270 nm to 310 nm. The rejection ratio increases to three decades when the photodiode is illuminated by intensity of 1 μW/cm^2, as a result of the increase of photocurrent above the absorption edge of $Al_{0.42}Ga_{0.58}N$. Using the data of photocurrent (I_{ph}), the responsivity ($\Re$) can be calculated as $\Re = I_{ph}/(PA)$, where P is the illumination power density and A is the active area. Because the photocurrent increases linearly with the illumination intensity, the responsivity remains almost constant in the measuring range of 10 nW/cm^2 to 1 μW/cm^2. It was found that the peak responsivity around 256 nm is about 44 mA/W by zero bias and increases to 51 mA/W by -5 V bias [Fig. 4.4(b)]. The corresponding external QE values are 21% and 25%, respectively.

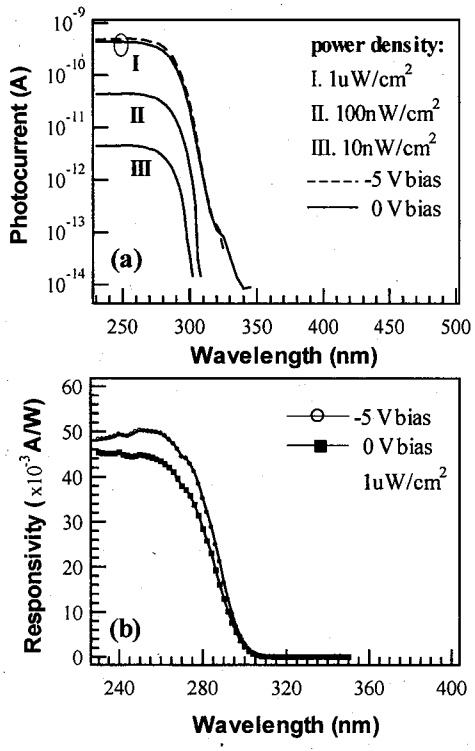

FIG.4.4. (a) Photocurrent spectra under the illumination of different incident power density; (b) Spectral responsivity of the AlGaN Schottky PDs at 0 V and -5 V bias, under an irradiation power density of 1 μW/cm^2.

For the solar-blind photodiode, the noise arising from the background radiation is far below that arising from the thermal agitation of carriers. The photodiode is then limited by thermal noise. With the zero-bias responsivity of $\Re$=21% and the resistance-area product of R_0A=6.4×10^{12} Ωcm^2, the detectivity D^* at room temperature (T=296 K) is evaluated as 7.9×10^{14} cmHz$^{1/2}$W^{-1}, a value even higher than those of the reported high performance solar-blind AlGaN p-i-n photodiodes [7], [15].

In this work, we fabricated the solar-blind AlGaN Schottky photodiodes grown on 4H-SiC substrates. The photodiodes show the leakage current density as low as 2.2×10^{-10} A/cm^2 at -5 V bias, which is ascribed to the high crystalline quality of the epitaxial structure

grown on 4H-SiC. Zero-bias peak responsivity of 44 mA/W was obtained at 256 nm under an illumination power density of 1 $\mu W/cm^2$, corresponding to an external QE of 21%. A rejection ratio of more than two orders of magnitude was achieved under the low intensity illumination of 10 nW/cm^2. A solar-blind detectivity was evaluated as 7.9×10^{14} $cmHz^{1/2}W^{-1}$ at 256 nm and zero bias.

4.3 AlGaN solar-blind Schottky photodiodes on AlN/sapphire templates

In developing high-performance AlGaN Solar blind photodiodes (SBDs), the substrate becomes a key factor concerning the epilayer quality and its influence on detector performance. In order to address the substrate issue for AlGaN epitaxy, various efforts have been taken to accommodate the mismatches. Significant improvement in dislocation density and detector characteristics have been shown by introducing epitaxial lateral overgrowth or low-temperature AlN interlayers [6,13]. We have also achieved the high-performance AlGaN Schottky SBDs fabricated on 4H-SiC substrate [16]. Compared with these approaches, the recently emerging technology of growing a thick AlN film (1μm) on *c*-plane sapphire, namely AlN/sapphire template, may provide a preferred solution for achieving high quality AlGaN epilayer [17,18]. High performance is then expected for the AlGaN SBDs based on AlN/sapphire template. In this section, we describe the growth, processing and characterization of the $Al_{0.42}Ga_{0.58}N$ solar-blind Schottky photodiodes on AlN/sapphire templates.

Photodiode structures were prepared by LP-MOCVD on 1-μm-thick AlN/sapphire templates. A 0.1-μm AlN transition layer was at first deposited. This layer is followed by a thin compositionally graded $Al_xGa_{1-x}N$ layer with Al compositions, x, from 0.7 to 0.4, a 1.0-μm-thick unintentionally doped $Al_{0.4}Ga_{0.6}N$ layer, a 0.8-μm-thick Si doped n^+-$Al_{0.42}Ga_{0.58}N$ ohmic-contact layer, and a 0.7-μm-thick unintentionally doped $Al_{0.42}Ga_{0.58}N$ active layer. The Al compositions of the AlGaN epilayers were determined XRD measurements. The structural properties investigated by XRD rocking curves show that the FWHM of the symmetric (0002) and asymmetric ($10\bar{1}2$) reflection peaks for the $Al_{0.42}Ga_{0.58}N$ epistructure were about 205 and 770 arcsec, respectively, as plotted in Fig. 4.5(b). An estimation using the method described in Ref. 19 shows that the $Al_{0.42}Ga_{0.58}N$

active layer is of high crystalline quality with a screw-TD density of ~7×10^7 cm^{-2} and an edge-TD density of ~~3×10^9 cm^{-2}. Observation with an atomic force microscope reveals that the surface morphology is free of crack with a roughness of about 0.43 nm across a 2×2 μm^2 scanning area.

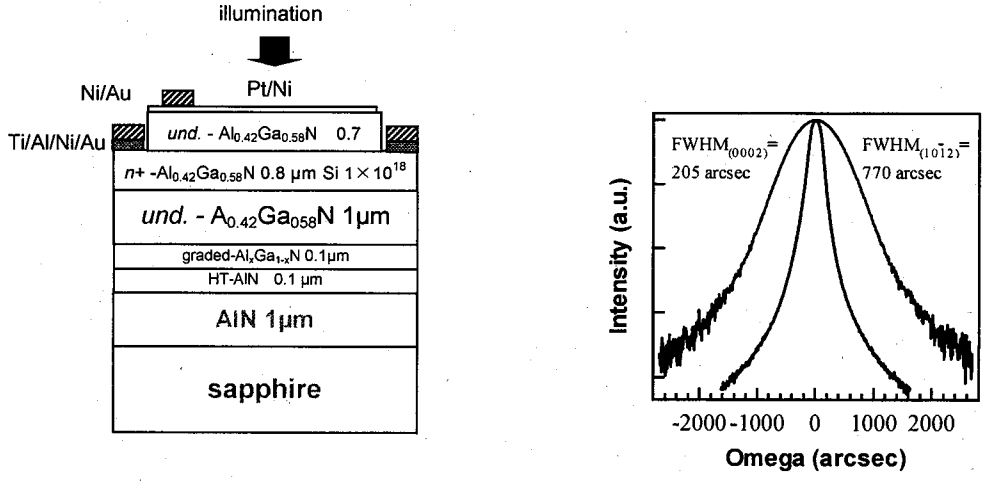

FIG. 4.5. (a) schematic structure of the $Al_{0.42}Ga_{0.58}N$ Schottky photodiodes on AlN/sapphire template. (b) XRD rocking curves of the (0002) and (10 $\bar{1}$ 2) omega scans for $Al_{0.42}Ga_{0.58}N$ layers.

Device processing was started by defining mesa structure with RIE method down to the n^+-$Al_{0.4}Ga_{0.6}N$ ohmic-contact layer. The plasma ambient was BCl_3 gas with a flow rate of 10 sccm under the pressure of 3 Pa and RF power of 10W. In order to remove the damages induced by RIE, the etched samples were treated in the boiling aqua regia for 10 min, rinsed in deionized water for 5 min and then annealed in N_2 ambient at 750 °C for 1min. Ohmic contacts of Ti/Al/Ni/Au (150 /850 /250 / 600 Å) were deposited by electron-beam evaporation, and annealed with a rapid thermal annealing (RTA) system at 850 °C for 30 s in N_2 ambient. For semitransparent Schottky contacts, Pt/Ni (60/20 Å) layers with area of 500×500 μm^2 were electron-beam deposited. Just prior to the vaccum evaporation, the samples were dippped in HCl:H_2O (1:1) solution, and reinsed in deionized water to cleaning the surface. Optical transmission analysis performed in wavelength range of 200 to 500 nm showed a flat spectral transmittance of the Pt/Ni contact ranging from about 36% to 43%. The fabrication of the devices was completed with the deposition of Ni/Au (25/200 nm) bilayer as bonding pads. A schematic structure of the device after the fabrication is shown in Fig. 4.5(a).

The fabricated photodiodes demonstrate very low dark current. As shown in Fig. 4.6, dark current as low as 40 fA was obtained at a typical reverse bias of 5 V, corresponding to a current density of 1.6×10^{-11} A/cm^2. This value is among the lowest values reported for AlGaN based photovoltaic diodes. The dark current exponentially increases with the reverse bias, but is only about 1.2 pA at the -10 V bias. In contrast to the reverse dark current, the photocurrent under the 260-nm monochromatic illumination is quite flat and at least one order of magnitude higher in the entire measured voltage range. It was also found that for most of the samples, the reverse breakdown voltages were around 25 V. Schottky contact parameters were extracted from the forward *I-V* curve by linear fitting based on the thermionic emission model. The resulting Schottky barrier height (SBH), ideality factor, and series resistance were 1.5 eV, 1.9 and 210 Ω, respectively. Also evaluated is the dynamic resistance at the zero-bias, R_0, which is deduced from $R_0=(dI/dV)^{-1}$ by exponential fitting to both the forward and reverse *I-V* curves [14]. The resulting value is $R_0=2.0\times10^{15}$ Ω, giving the product of $R_0A=5.0\times10^{12}$ Ωcm^2, where A is the contact area of Schottky electrode.

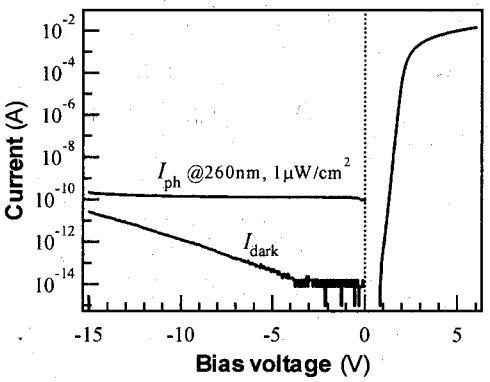

FIG. 4.6. *I-V* curves of the $Al_{0.42}Ga_{0.58}N$ Schottky photodiode taken in dark and under illumination.

C-V characteristics were recorded using a HP4284 LCR meter at 100 kHz. In Fig. 4.7(a), the *C-V* and 1/C^2-V plots of a typical photodiode are presented. The 1/C^2-V relation gives a SBH of 1.8 eV and an average net carrier concentration of 2.8×10^{16} cm^{-3} for the AlGaN active layer. The SBH determined from the *C-V* data is 0.3 eV larger than that from the *I-V* analysis. Moreover, the ideality factor is much larger than unity

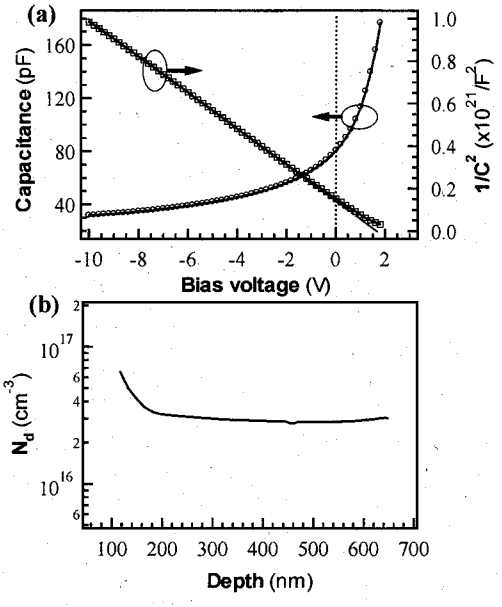

FIG. 4.7. (a) *C-V* and *1/C^2-V* dependences of the $Al_{0.42}Ga_{0.58}N$ Schottky photodiode; (b) Carrier concentration (N_{c-v}) profile determined by *C-V* measurements.

despite the low net carrier concentration. These results suggest that the current transport in our devices involves mechanisms other than thermionic emission. In Fig. 4.7 (b), the depth profile of net carrier concentration derived from *C-V* curve is shown. It is seen that the carrier concentration of the active layer remains roughly constant in the region deeper than ~200 nm and gradually increases toward the surface. Such an increase of the carrier concentration near the surface has been reported due to the shallow oxygen donors, which are easily incorporated at the surface of MOCVD-grown AlGaN layer with high Al composition [20,21]. We speculated that the nonideal *I-V* behavior with the large ideality factor is caused by the heavily doped surface region resulting from these donor impurities. A further improvement in the device performance such as leakage current and reverse breakdown voltage can be expected by reducing these unintentional surface donors.

Figure 4.8 demonstrates the spectral responses of the $Al_{0.42}Ga_{0.58}N$ Schottky photodiodes. The photoresponse measurements were carried out in the wavelength range of 200 to 500 nm. As seen from the plots in the Fig. 4.8(a), the spectral photocurrent begins to cut off at around 284 nm, which is 80% drop-off from the peak value. A rejection ratio of more than two orders of magnitude was observed between 270 and 300 nm at a low illumination intensity of 10 nW/cm^2. Increasing the illumination intensity leads to an increase of the spectral photocurrent above the $Al_{0.42}Ga_{0.58}N$ band edge. Consequently, the rejection ratio rises to four orders of magnitude when the photodiode is illuminated at 1μw/cm^2 intensity. In Fig. 4.8(b) the responsivity spectra calculated from the measured spectral photocurrents are shown. Since the photocurrent increases linearly with the illumination intensity, the solar-blind responsivity keeps nearly constant for the intensity from 10 nW/cm^2 to 1μw/cm^2. Under the 1μw/cm^2 illumination, a zero-bias peak responsivity of 41 mA/W is observed at 256 nm, corresponding to an external

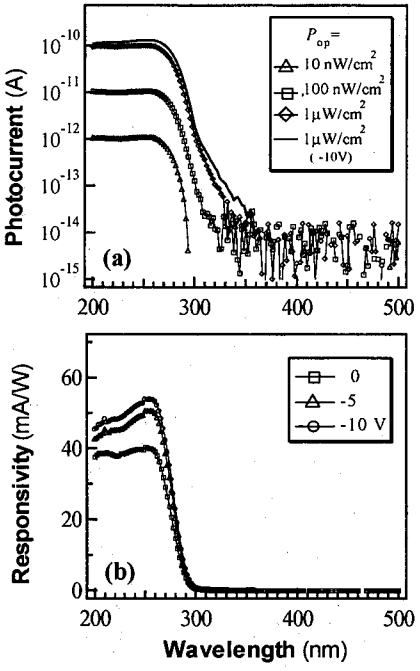

FIG. 4.8. (a) Photocurrent spectra taken under the different illumination power density; (b) Spectral responsivity of the $Al_{0.42}Ga_{0.58}N$ Schottky photodiode biased at 0, -5 and -10 V.

QE value of 20 %. The responsivity increases with the reverse bias and reaches to 54 mAW (external *QE* =26%) at -10 V. With the consideration that for solar-blind photodiodes the limiting source of noise is thermal noise, the specific detectivity, D^*, of our devices operating in the photovoltaic mode (without bias) can be estimated from the obtained values of R_0A and zero-bias responsivity. The then calculated D^* values are found to be higher than 2.5×10^{14}cmHz $^{1/2}$/W in the region from 200nm to 280nm and with a maximum of 7.0×10^{14}cmH$^{1/2}$/W at 256 nm at a room temperature of 298K.

In summary, the high-performance $Al_{0.42}Ga_{0.58}N$ solar-blind Schottky photodiodes were fabricated on AlN/sapphire template. The solar-blind photodiodes exhibited very low dark current, which is 40 fA at 5 V reverse bias. A rejection ratio of two orders of magnitude by 300 nm is observed even under a very weak irradiation density of 10 nW/cm^2. The peak external QE is 20% by zero-bias and increases to 26% by 10 V bias at 256 nm. R_0A product of 5.0×10^{12} Ωcm^2 was obtained, leading to a high specific detectivity of $D^*=7.0\times10^{14}$cmH$^{1/2}$/W at 256 nm.

To investigate the response characteristics of the $Al_{0.42}Ga_{0.58}N$ Schottky SBDs to lighter flame, we fabricated large-size $Al_{0.42}Ga_{0.58}N$ Schottky SBDs with an active area of 2×2 mm^2. The large active area SBDs can provide high photocurrent, making us easy to identify the detector signals. The completed prototype devices are shown in Fig. 4.9(a). Dark current density as low as 6.6×10^{-11} A at -5 V bias was obtained [Fig.4.9(b)]. Peak responsivity for

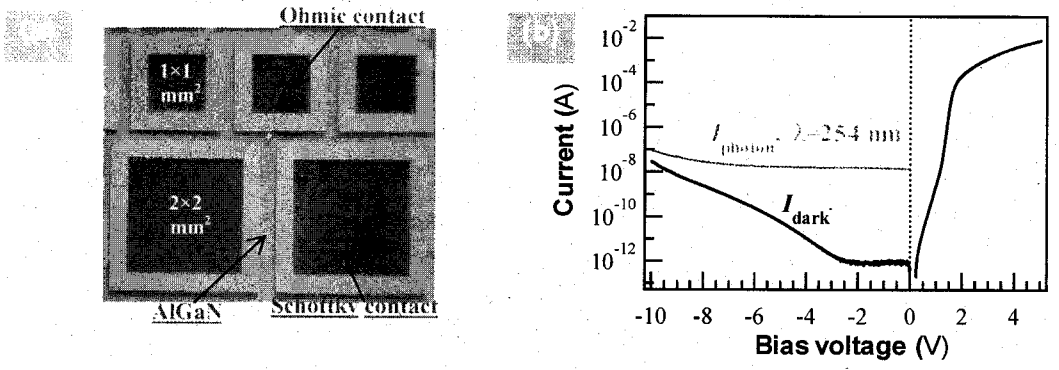

FIG. 4.9. (a) photograph of the large-size $Al_{0.42}Ga_{0.58}N$ SBD with active area of 2×2 mm^2. (b) *I-V* curves of the large-size $Al_{0.42}Ga_{0.58}N$ SBD under the dark and illumination conditions.

zero bias is measured to be 38 mA/W at 260 nm, giving the external QE of 18%. The value for estimated detectivity is 1.2×10^{14} cmHz$^{1/2}$W^{-1}.

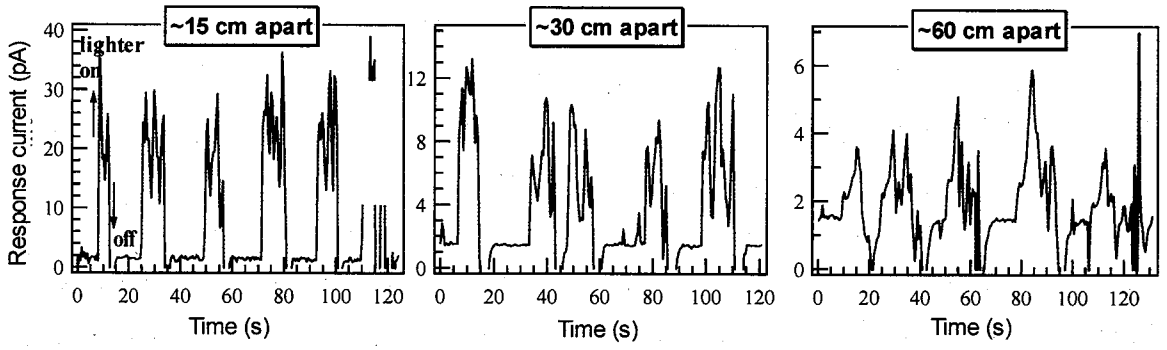

FIG. 4.10. The responses (photocurrents) of the $Al_{0.42}Ga_{0.58}N$ Schottky SBD to the lighter flame placed at distances of 15, 30, and 60 cm from the detector.

By using this device, the experiment to verify the detection of lighter flame was conducted under a fluorescent room light. Flame signal of ~30 pA was observed when the lighter was set ~15 cm apart from the detector (as shown in Fig. 4.10). The signal decreased to ~5 pA when the separation distance was increased to 60 cm, which because the UV irradiation from the lighter flame was strongly absorbed by air. It was also found that the effect of room light is negligible for this $Al_{0.42}Ga_{0.58}N$ Schottky SBD. From a practical view point, however, the flame signal delivered by our device is still too low for the resolution of photodiode preamplifier. Besides, with the consideration of cost/benefit tradeoff, the active area of our AlGaN SBD is expected to be equal to or smaller than 1×1 mm^2. Assuming an active area of $1mm^2$ and a detector-lighter separation of 5 m, it is estimated that a solar-blind responsivity of at least 10 A/W is needed for our devices to work as flame detector [22]. This means that an internal gain of ~ 300 is required for AlGaN SBD. To achieve such an internal gain, one of the solutions is to develop AlGaN based solar-blind avalanche photodiode (APD). To date, a major obstacle in achieving AlGaN solar-blind APD is the premature microplasma breakdown before the electric field reaches the level of bulk avalanche breakdown. Compared with Schottky-barrier photodiodes, the *p-i-n* junction photodiodes are generally suitable for high-voltage applications, because of the high breakdown voltage. According to this, the next subject of our research effort was decided to develop AlGaN solar-blind *p-i-n* photodiodes with high performances in terms of low dark current, high breakdown voltage, and high responsivity. Ultimately, the final goal of our

research is to fabricate AlGaN solar-blind APD with multiplication gain of higher than 300, based on the structure of high-performance solar-blind *p-i-n* photodiodes.

4.2 AlGaN solar-blind *p-i-n* photodiodes

Currently, a research focus on the AlGaN SBDs is the *p-i-n* structure photodiode, attracted by the advantages of high breakdown voltage, low dark current, and high quantum efficiency [6,13,23,24]. In the past few years, the advances in the AlGaN *p-i-n* SBDs have led to the realization of high performances such as low dark current density on the order of 10^{-11} A/cm^2 at -5V bias [7,15], high quantum efficiency of 53% at zero-bias [7], and high detectivity of 4.9×10^{14} cmHz$^{1/2}$/W [15]. In spite of these impressive results, the development of high-quality AlGaN *p-i-n* SBDs still remains challenges. The lack of suitable lattice- and thermal-matched substrates causes the high defect density in the $Al_xGa_{1-x}N$ ($x \geq 0.4$) epilayers and impedes the device performance. Moreover, for p-type AlGaN epilayers, the activation energy of p-type doptant increases with the Al composition, making the p-type doping of high Al-content AlGaN difficult. In our previous works, we have demonstrated the high quality solar-blind AlGaN Schottky photodiodes fabricated on substrates of 4H-SiC and AlN(~ 1 μm)/sapphire template [16,28]. We report, in this section, the high performance solar-blind $Al_{0.45}Ga_{0.55}N$ *p-i-n* photodiodes fabricated on AlN/saaphire templates.

The growth was initiated by the deposition of a tri-layer structure comprised of a 100-nm homoepitaxial AlN layer, a thin compositionally graded $Al_xGa_{1-x}N$ layer, and a 1.0-μm-thick unintentionally doped $Al_{0.45}Ga_{0.55}N$ layer, aiming to improve the overall crystalline quality and reduce the threading dislocations running into the subsequent layers. Next, the *p-i-n* structure was grown, consisting of a 0.5-μm-thick heavily Si-doped (N_D~3×10^{18} cm^{-3}) n^+-$Al_{0.45}Ga_{0.55}N$ layer, a 0.2-μm-thick unintentionally doped $Al_{0.45}Ga_{0.55}N$ layer, and a 30-nm-thick *p*-$Al_{0.45}Ga_{0.55}N$ layer. The structure was terminated with an Mg-doped graded $Al_xGa_{1-x}N$ layer followed by a p^+-GaN (N_A~2×10^{20} cm^{-3}) layer to facilitate *p*-type ohmic contact. For the *p*-type layers, the activation of the Mg dopant was carried out by thermal annealing at 800 °C for 30 min with N_2 gas flowing. The root mean square (RMS) value of the surface roughness measured by atomic force microscopy (AFM) was less than 1 nm over a 3 μm×3 μm area. HRXRD analysis shows that the FWHMs of the (0004) ω- and ω-2θ-scan for the $Al_{0.45}Ga_{0.55}N$ epilayers are 142 and 151 arcsec, respectively. Such low

FWHM values benefit from the AlN/sapphire template which provides good lattice and thermal matching with the subsequent AlGaN layers. The screw TD density deduced from the XRD data is ~4×10^7 cm^{-2}[19], denoting that this epistructure is of sufficiently high crystalline quality to fabricate high performance device [13,29].

Figure 4.11 depicts the schematic structure of a completed device. Standard processing techniques were employed for the device fabrication, including photolithography, dry etch, electron-beam and thermal evaporation, and lift off. Mesas with the area ranging from 0.08 to 0.27 mm^2 were defined RIE method to the n^+-$Al_{0.45}Ga_{0.55}N$ layer. To recover the damages caused by RIE, the etched samples were treated by a procedure described in the previous section. Ti/Al/Ni/Au and Ni/Au metallizations, thermally annealed in N_2 ambient at 850 and 550 °C, were utilized to provide the *n*-type and *p*-type ohmic contacts, respectively. Ni/Au layers of ~500 nm thickness were deposited on the top of two-type ohmic contacts as contact pads.

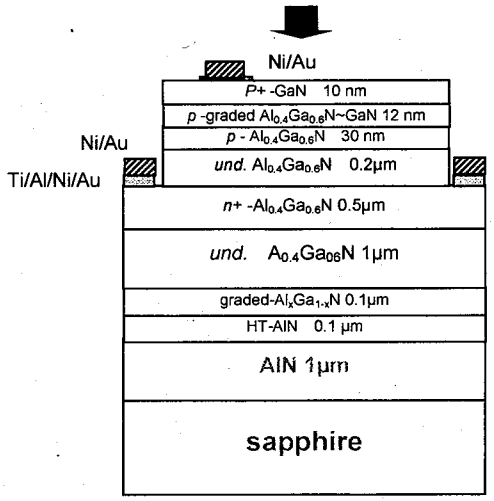

FIG. 4.11. Schematic cross-sectional structure of the $Al_{0.45}Ga_{0.55}N$ solar-blind *p-i-n* photodiode.

In Fig. 4.12, the dark *I-V* characteristics of a solar-blind *p-i-n* photodiode are presented. From the forward region, we obtained an ideality factor of n=2.13 and a series resistance of R_s=194 Ω, suggesting a high quality *p-i-n* junction in which the current transport mechanism is governed by recombination. The forward turn-on voltage is about 5.4 V, as shown in the inset of Fig. 4.12. Very low dark currents were observed in the fabricated photodiodes. Leakage (dark) current of only 70 fA was obtained at a reverse bias of 5 V, which corresponds to a current density of 2.6×10^{-11} A/cm^2. The dark current remains

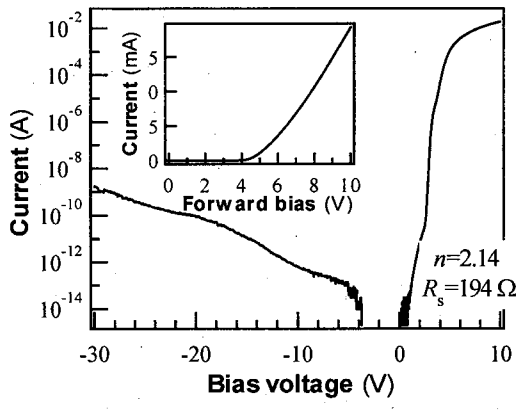

FIG. 4.12. Dark *I-V* characteristics of the 520×520 μm^2 active-area $Al_{0.45}Ga_{0.55}N$ *p-i-n* photodiode fabricated on AlN/sapphire template. The inset displays the linear-scale forward *I-V* curve.

less than 1pA up to -10 V and less than 2 nA up to -30 V bias. The dynamic resistance of the photodiode, defined as $R = dV/dI$, is larger than 10^9 Ω in the measured reverse bias range. By fitting to the forward and reverse *I-V* curves, we obtained the value of dynamic resistance at zero bias as R_0=7.9×10^{14} Ω, yielding a dynamic resistance-area product of R_0A= 2.1×10^{12} Ωcm^2. To investigate the processing effect on the dark current, the dependence of dark current density on perimeter to area (P/A) ratio was examined (Fig. 4.13). It is clear that the dark current density is nearly constant with varying perimeter-to-area ratio, indicating that the mesa-sidewall leakage is not significant in our devices. The low leakage current of the photodiodes, we suggest, is due mainly to the low TD density in the AlGaN epilayers and the high quality *p-i-n* junction.

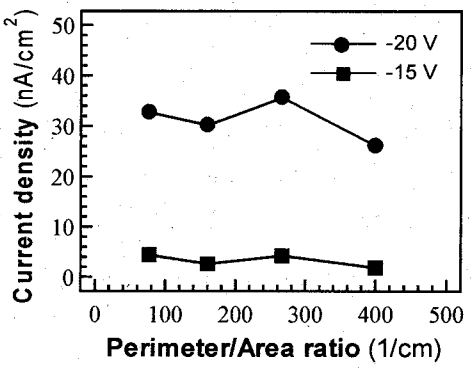

FIG. 4.13. Dependence of the dark current density in the *p-i-n* photodiodes on the perimeter to area ratio.

Spectral photoresponses of an $Al_{0.45}Ga_{0.55}N$ solar-blind *p-i-n* photodiode with 520×520 μm^2 active area are shown in Fig. 4. Each tested device was uniformly illuminated from the top side. The photocurrent was measured as the difference between the currents under the illumination and in the dark. In the case of 1μw/cm^2 illumination, it was observed that the photocurrent of the zero-biased photodiode, Fig. 4.14(a), reaches a peak at ~258 nm and falls by two and four orders of magnitude from the peak value by 290 nm and by 310 nm, respectively. We ascribed the high rejection ratio to the high UVC photoresponse and the low dark current. It is shown that increasing the reverse bias to 15 V results in a decrease of the rejection ratio as the noise associated with dark current increases. Also, the rejection ratio reduces with the weakening of illumination intensity as the UVC photocurrent decreases. The photocarriers generated in the p^+-GaN cap layer were found not to significantly contribute to the photocurrent, which is due primarily to the block by the band offset at *p*-type GaN/AlGaN interface. As shown in Fig. 4b, the zero-bias peak responsivity is evaluated as 63 mA/W at 258 nm, which corresponds to an external quantum efficiency (QE) of ~30 %. This high external QE value may be attributed to the thin p^+-GaN cap layer used in our *p-i-n* junction structure and the low defect density in the AlGaN epilayers, as

compared to those values reported in Ref. 4 and Ref. 8. The peak responsivity reaches 82 mAW (external QE~39%) when the device is biased at -15 V, due to the extension of depletion region. The upper-bound specific detectivity D^* estimated from the R_0A product and zero-bias responsivity is shown to be 7.1×10^{14} cmHz$^{1/2}$/W at 258 nm.

In summary, high quality $Al_{0.45}Ga_{0.55}N$ solar-blind *p-i-n* photodiodes on AlN/sapphire template have been fabricated. Dark current as low as ~ 70 fA was achieved at -5 V bias for the 520×520 μm^2 mesa area devices. The peak external QE at 258 nm is 30% by zero-bias and increases to 39% by 20 V bias. A rejection ratio of two orders of magnitude by 290 nm is observed under a weak irradiation density of 1 μW/cm^2. At room temperature, the upper-bound detectivity is about 7.1×10^{14} cmHz$^{1/2}$/W at 258 nm.

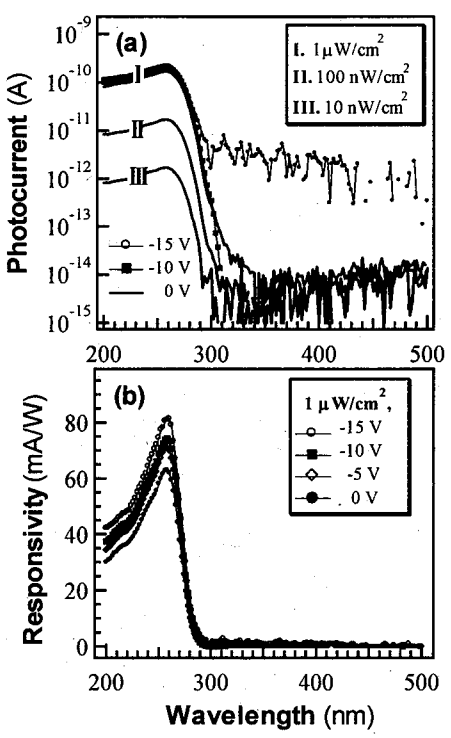

FIG. 4.14. Photoresponse spectra of a representative $Al_{0.45}Ga_{0.55}N$ *p-i-n* photodiode with an active area of 520×520 μm^2

However, a drawback of the $Al_{0.45}Ga_{0.55}N$ *p-i-n* SBDs presented above is the premature breakdown or the soft breakdown (large increase in the leakage current) occurs at a low voltage, typically lower than 40 V. Repeated experiments demonstrate the identical behavior of the breakdown voltage. Since in our $Al_{0.42}Ga_{0.58}N$ Schottky SBDs, we have achieved breakdown voltages of more than 50 V, it can be inferred that this low-voltage breakdown in the *p-i-n* SBDs may not result from processing during device fabrication or from *i*-and *n*-type $Al_{0.45}Ga_{0.55}N$ layers. It is most likely related to the *p*-type layers due to the low doping efficiency and high density of defects. For solving this problem, we changed the thickness of the p^+-GaN cap layer to investigate its effect on the breakdown voltage and leakage current.

The four samples under investigation have the same epilayer structure except for the thickness of the p^+-GaN cap layer (10, 20, 35, and 50 nm), as shown in Fig. 4.15(a). The experimental procedure was carried out according to the method described above in this section. For the photodiodes with the cap layers thicker than 10 nm, recess etch was

performed to reduce the strong absorption of the top UV illumination. The RIE recipe used for recess etch was identical to that for *n*-type ohmic contact. The etching depths of the 20-nm, 35-nm, and 50-nm cap layers were approximately 15, 30, and 45 nm, respectively.

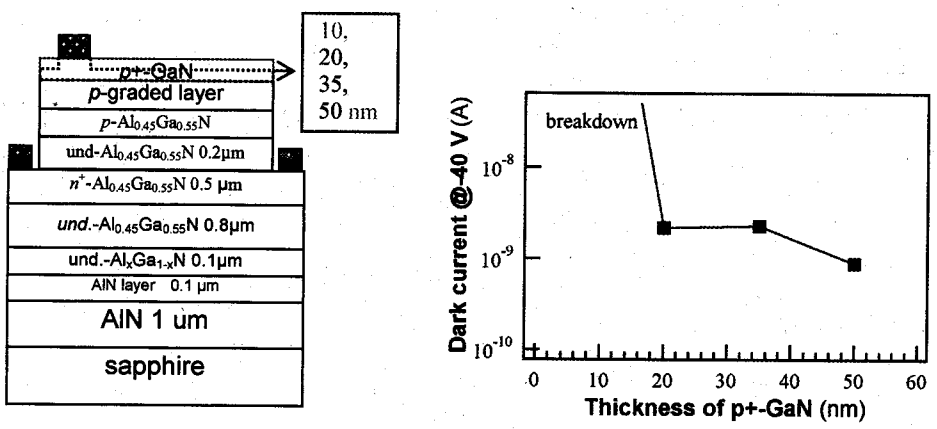

FIG. 4.15. (a) Schematic cross-sectional structure of the $Al_{0.45}Ga_{0.55}N$ *p-i-n* SBDs with p^+-GaN cap layers of different thicknesses. (b) The dependence of the dark current at -40 V bias on the thickness of the p^+-GaN cap layer.

It was found, as shown in Fig. 4.15(b) that there is a trend towards lower dark (leakage) current (at -40 V bias) with thicker p^+-GaN cap layer. Strong breakdown was not observed in the devices with thicker cap layers (>10 nm) up to bias voltage of -200 V.

For investigating the avalanche multiplication effect at the high reverse biases in the $Al_{0.45}Ga_{0.55}N$ *p-i-n* SBDs, we performed more detailed measurements on the photodiodes with the p^+-GaN cap layer thickness of 35 nm.

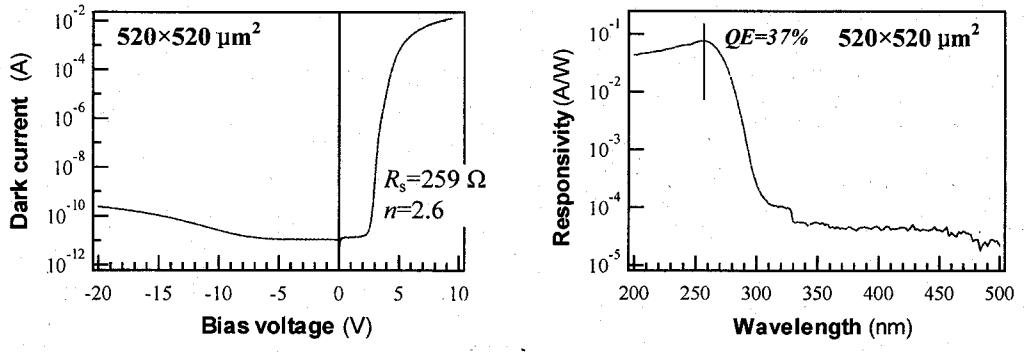

FIG. 4.16. (a) Dark *I-V* curves of the $Al_{0.45}Ga_{0.55}N$ *p-i-n* SBD with a p^+-GaN cap layer of 35 nm. (b) Spectral responsivity of the *p-i-n* SBD measured under the zero bias..

Dark forward and reverse *I-V* curves of the device with a 35-nm cap layer are shown in Fig. 4.16(a). The ideality factor, *n*, of this *p-i-n* photodiode was found to be 2.61 and the series resistance, R_s, was ~259 Ω. Under -5 V bias, the measured dark current is about 49 pA,

corresponding to a current density of 1.8×10^{-8} A/cm^2. The reason for the increase in the leakage current, as compared with that obtained in the photodiodes with a 10-nm thick p^+-GaN cap layer (2.6×10^{-11} A/cm^2 at -5 V bias), is not very clear at present. A possible factor responsible for this leakage increase may be the surface recombination current resulting from the surface defects induced by the dry etching (RIE) process. For most of the samples, no breakdown was observed at high reverse biases, up to the limit of our instrument (200 V).

Spectral responsivity of the $Al_{0.45}Ga_{0.55}N$ *p-i-n* SBD at zero bias is shown in Fig. 4.16(b). The peak external QE is 37% at 256 nm (the corresponding responsivity is 77.4 mA/W). This value is about 7% higher than that obtained in the device with a 10-nm thick p^+-GaN cap layer, which is ascribed to the recess etch of the p^+-GaN cap layer. Shown in Fig. 4.17 is the reverse I-V characteristics measured under the dark and UV illumination at a wavelength of 254 nm. In the low reverse bias region from 10 to 60 V, the photocurrent remains nearly constant indicating a unity-gain behavior. After 60 V bias, the avalanche gain becomes obviously visible. The multiplication gain (M) was determined using the photocurrent at -10 V bias as the unity-gain reference point. The maximum avalanche gain is about 49 at 98 V reverse bias. At biases higher than 98 V, the avalanche gain decreases due to the rapid increment in the dark current. Unfortunately, Geiger mode breakdown was not observed in the fabricated device. Besides, the relatively high leakage (dark) current density is needed to be reduced to a level of 10^{-11} A/cm^2. These suggest that further investigation on the optimization of device structure and the improvement of crystal quality are necessary in our future works.

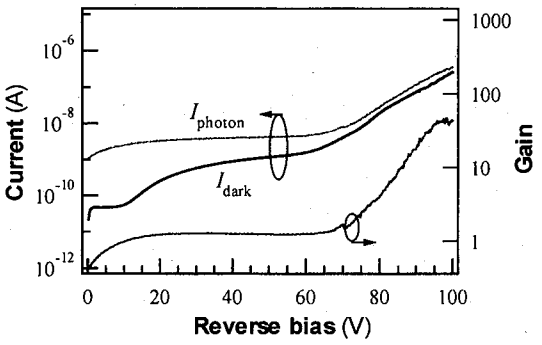

FIG. 4.17. Reverse *I-V* characteristics under the dark and illumination (λ=254 nm) and the multiplication gain as a function of the bias voltage (right axis).

References

1. B. Heying, X. H. Wu, S. Keller, Y. Li, D. Kapolnek, B. P. Keller, S. P. DenBaars, and J. S. Speck: Appl. Phys. Lett. **68** (1996) 643.
2. M. Razeghi and A. Rogalski: J. Appl. Phys. **79** (1996) 7433.
3. J. C. Campbell, C. J. Collins, M. M. Wong, U. Chowdhury, A. L. Beck, and R. D. Dupuis: Phys. Stat. Sol. A. **188** (2001) 283.
4. E. Muñoz, E. Monroy, J.L. Pau, F. Calle, F. Omnès, and P. Gibart: J. of Phys. : Cond. Matter. **13** (2001) 7115.
5. J. C. Carrano, T. Li, P. A. Grudowski, R. D. Dupuis, and J. C. Campbell: IEEE Circuits Devices Mag. **15** (1999) 15.
6. C. Pernot, A. Hirano, M. Iwaya, T. Detchprohm, H. Amano and I. Akasaki: Jpn. J. Appl. Phys. **39** (2000) L387.
7. C. J. Collins, U. Chowdhury, M. M. Wong, B. Yang, A. L. Beck, R. D. Dupuis, and J. C. Campbell: Appl. Phys. Lett. **80** (2002) 3754; C. J. Collins, U. Chowdhury, M. M. Wong, B. Yang, A. L. Beck, R. D. Dupuis, and J. C. Campbell: Electron. Lett. **38** (2002) 824.
8. N. Biyikli, O. Aytur, I. Kimukin, T. Tut, and E. Ozbay: Appl. Phys. Lett. **81** (2002) 3272.
9. N. Biyikli, I. Kimukin, T. Kartaloglu, O. Aytur, and E. Ozbay: Appl. Phys. Lett. **79** (2003) 2334.
10. J. D. Brown, J. Matthews, S. Harney, J. C. Boney, J. F. Schetzina, J. D. Benson, K. V. Dang, T. Nohava, W. Yang, and S. Krishnankutty: MRS Internet J. Nitride Semicond. Res. **5S1** (2000) W1.9.
11. T. Li, D. J. H. Lambert, A. L. Beck, C. J. Collins, B. Yang, M. M. Wong, U. Chowdhury, R. D. Dupuis, and J. C. Campbell: Electron. Lett. **36** (2000) 1581.
12. J. T. Torvik, J. I. Pankove, S. Nakamura, I. Grzegory, and S. Porowski:J. Appl. Phys. **86** (1999) 4588.
13. G. Parish, S. Keller, P. Kozodoy, J. P. Ibbetson, H. Marchand, P. T. Fini, S. B. Fleischer, S. P. DenBaars, and U. K. Mishra: Appl. Phys. Lett. **75** (1999) 247.
14. C. J. Collins, T. Li, D. J. H. Lambert, M. M.Wong, R. D. Dupuis, and J. C. Campbell: Appl. Phys. Lett. **77** (2000) 2810.

15. N. Biyikli, I. Kimukin, O. Aytur, and E. Ozbay: IEEE Photon. Technol. Lett. **16** (2004) 1728.
16. H. Jiang, T. Egawa, and H. Isikawa: IEEE Photon. Technol. Lett. **18** (2006) 1353.
17. T. Shibata, K. Asai, S. Sumiya, M. Mouri, M. Tanaka, O. Oda, H. Katsukawa, H. Miyake, and K. Hiramatsu: Phys. Status Solidi C **0** (2003) 2023.
18. N. Kuwano, T. Tsuruda, Y. Kida, H. Miyake, K. Hiramatsu, T.Shibata: Phys. Status Solidi C **0** (2003) 2444.
19. H. Jiang, T. Egawa, M. Hao and Y. Liu: Appl. Phys. Lett. **87** (2005) 241911.
20. J. K. Kim, H. W. Jang, and J. L. Lee: J. Appl. Phys. **94** (2003) 7201.
21. J. Kotani, M. Kaneko, H. Hasegawa, and T. Hashizume: J. Vac. Sci. Technol. B **24** (2006) 2148.
22. M. Tanaka: Research Presentation 060612, Intellectual Cluster Headquarters, Aichi Science & Technology Foundation.
23. D. Walker, V. Kumar, K. Mi, P. Sandvik, P. Kung, X. H. Zhang, and M. Razeghi: Appl. Phys. Lett. **76** (2000) 403.
24. J. D. Brown, J. Li, P. Srinivasan, J. Matthews, and J. F. Schetzina: MRS Internet J. Nitride Semicond. Res. **5** (2000) 9.
25. C. J. Collins, U. Chowdhury, M. M. Wong, B. Yang, A. L. Beck, R. D. Dupuis, and J. C. Campbell: Appl. Phys. Lett. **80** (2002) 3754.
26. C. J. Collins, U. Chowdhury, M. M. Wong, B. Yang, A. L. Beck, R. D. Dupuis, and J. C. Campbell: Electron. Lett. **38** (2002) 824.
27. N. Biyikli, I. Kimukin, O. Aytur, and E. Ozbay: IEEE Photon. Technol. Lett. **16** (2004) 1718.
28. H. Jiang and T. Egawa: Appl. Phys. Lett. **90** (2007) 121121.
29. J. W. P. Hsu, M. J. Manfra, D. V. Lang, S. Richter, S. N. G. Chu, A. M. Sergent, R. N. Kleiman, L. N. Pfeiffer, and R. J. Molnar: Appl. Phys. Lett. **78** (2001)1685.

5. Summary

This research project is devoted to the development of high-performance $Al_xGa_{1-x}N$ ($0 \le x \le 1$) UV photodetectors for flame sensing. Studies have been performed on the LP-MOCVD epitaxy growth, fabrication and characterization of AlGaN MSM, Schottky barrier, and *p-i-n* junction photodiodes. AlGaN based UVA, UVB, and UVC (solar blind) photodiodes with low dark current and high detectivity have been successfully developed.

In the first phase of this project, by employing Ir/Ni/Ir electrode, we have achieved low dark current density of 1.8×10^{-10} A/cm^2 at -5 V bias and high detectivity of 5.8×10^{15} cm $Hz^{1/2}W^{-1}$ at 345 nm in the GaN UVA Schottky photodiodes on sapphire substrates.

To fabricate AlGaN UVB photodiodes, high-quality $Al_xGa_{1-x}N$ active layer with Al composition of $x>0.2$ is necessary. It has been found that epitaxial AlGaN layers with low defect density are of great importance for the success of UV photodiodes. In this research phase, AlN/sapphire templates were introduced to be used as the substrate for growing thick, crack free and high-crystalline quality $Al_{0.23}Ga_{0.77}N$ epilayers. High quality $Al_{0.23}Ga_{0.77}N$ layers with reduced dislocation density have been obtained by inserting a thin HT GaN layer between the AlGaN layer and AlN/sapphire template. The UVB Schottky photodiodes fabricated on these low-dislocation-density $Al_{0.23}Ga_{0.77}N$ layers demonstrated low dark current of 3.3×10^{-10} A/cm^2 at -5 V bias and zero-bias external QE of 23.5% at 310 nm. Using a large active area (4×4 mm^2) UVB Schottky photodiode fabricated on the same epistructure, we have detected the UV signal from the lighter flame. The detector response to the room light was also observed. Consequently, solar-blind photodiode is expected to eliminate the effect of this background noise.

High-performance solar-blind $Al_{0.42}Ga_{0.58}N$ Schottky photodiodes were fabricated both on AlN templates and 4H-SiC substrates. A HT-AlN transfer layer and a graded $Al_xGa_{1-x}N$ layer were introduced to improve the crystalline quality of the $Al_{0.42}Ga_{0.58}N$ epilayers. The resulting photodiodes demonstrated a solar blind detectivity as high as 7.9×10^{14} cm$Hz^{1/2}$/W. This is the highest value of detectivity reported for AlGaN solar-bind detectors (SBDs). A summary of the photodiode performance parameters for the AlGaN SBDs reported by our and other research groups is listed in Table 5.1. To investigate the response characteristics to the lighter flame, we used an $Al_{0.42}Ga_{0.58}N$ Schottky SBD with 2×2 mm^2 active area to

detect the flame signal. The $Al_{0.42}Ga_{0.58}N$ photodiode demonstrated a photocurrent of about 6 pA when placed 60 cm apart from the lighter. It was also found that the effect of the fluorescent room light is negligible for our solar-blind device. However, from a practical application view, the photocurrent is still too low and an internal gain of at least 300 is needed. As a final goal, we decided to develop AlGaN solar-blind avalanche photodiodes with multiplication gain larger than 300.

Our attempt to fabricate AlGaN solar-blind APDs was based on the structure of the high-performance *p-i-n* SBD (see Table 5.1). A 35-nm thick p^+-GaN layer was capped on the top of the *p-i-n* structure to improve the breakdown voltage. The resulting devices exhibit linear-mode avalanche gain of about 49 at -98 V bias. Geiger mode avalanche breakdown was not found in the devices. Besides, the dark current was relatively high (1.8×10^{-8} A/cm^2 at -5 V bias), which may result from the surface recombination current related to the RIE (recess etch) induced defects.

These results suggest that, for fabricating high-performance AlGaN solar-blind APDs being used as flame sensor, more efforts are required in optimizing the growth conditions and procedure to decrease the density of the line and point defects present in the AlGaN layers and improving *p*-type doping efficiency.

TABLE 5.1. Summary of the photodiode performance parameters for AlGaN Schottky and *p-i-n* SBDs reported by the leading research groups.

Research Groups	**detector structure**	**cutoff wavelength** (nm)	**active area** (mm^2)	**dark current** J_d **@-5 V** (A/cm^2)	**external** ***QE*** **@ 0 V** (%)
Bilkent University, Turkey *Appl. Phys. Lett. 82, 2344 (2003).*	Schottky	274	0.0225	$7\sim18\times10^{-10}$	5
	PIN	283	0.01	3.0×10^{-11}	30
University of Texas, Austin, USA *Appl. Phys. Lett. 80, 3754 (2002).*	PIN	280	0.05	8.2×10^{-11}	53
Meijo University & Osaka gas Ltd. Japan *Jpn. J. Appl. Phys. 39, L387 (2000).*	PIN	270	2.5	3.5×10^{-9}	5.5
			0.07	4.0×10^{-10}	
Nagoya Institute of Technology	Schottky	276	4.0	2.1×10^{-9}	21
			1.0	2.0×10^{-10}	21
			0.25	1.6×10^{-11}	21
	PIN	273	0.27	2.6×10^{-11}	22
			0.27	1.8×10^{-8}	37